minerals

MDPI

Article

Geochemical Characteristics and Geological Significance of Late Cretaceous to Paleocene Intermediate–Acidic Intrusive Rocks in the Qiuwo Area, Southern Margin of the Lhasa Terrane, China

Min Jia [1], Fuwei Xie [1,*], Yibin Lin [2], Shuyuan Chen [2], Yang Yang [2] and Jiancuo Luosang [2]

[1] College of Earth and Planetary Sciences, Chengdu University of Technology, Chengdu 610059, China
[2] Tibet Xianglong Mining Co., Ltd., Xigaze 858500, China
* Correspondence: xiefuwei19@cdut.edu.cn

Abstract

The Late Cretaceous to Paleocene magmatic evolution along the southern margin of the Lhasa Terrane records a critical transition from oceanic subduction to continental collision, yet its western segment remains underexplored. This study presents integrated petrographic, zircon U–Pb geochronological, zircon Hf isotopic, whole-rock geochemical, and Sr–Nd isotopic data for three distinct phases of intermediate to felsic intrusions from the Qiuwo area in the western segment of the southern Lhasa terrane. The results reveal three distinct magmatic pulses: an early granodiorite emplaced at 89.9 ± 0.75 Ma, followed by a diorite crystallizing at 68.6 ± 0.56 Ma, and a late-stage granodiorite forming at 56.75 ± 0.43 Ma. All three rock units are metaluminous to weakly peraluminous (A/CNK < 1.1), sodic (Na_2O > 3.2 wt.%), and dominated by amphibole, with zircon saturation temperatures of 737–786 °C, consistent with I-type granitoid affinity. All units are metaluminous (A/CNK = 0.92–1.00), calc-alkaline to high-K calc-alkaline, and enriched in LILE (K, Th, Rb) while depleted in HFSE (Nb, Ta, P, Ti), with moderate ΣREE (81–130 ppm), elevated $(La/Yb)_N$ (9.3–15.8), and negative Eu anomalies (δEu = 0.70–0.89). The early granodiorite is Na-rich (Na_2O/K_2O = 1.6), whereas the Paleocene granodiorite shows elevated K_2O (3.2 wt.%) and reduced Na_2O/K_2O (~1.0), reflecting progressive crustal thickening and increasing magmatic differentiation. Zr and Hf are relatively enriched, and Sr/Y ratios decrease from 39 to 21, consistent with evolving magmatic conditions from deeper crustal melting in the Late Cretaceous to shallower, more evolved sources in the Paleocene. Zircon Hf isotopes reveal consistently positive εHf(t) values (+10.4 to +4.9), indicating derivation from juvenile basaltic lower crust. Sr–Nd isotopic data further demonstrate a systematic evolution: εNd(t) decreases from +2.7 to −0.1, while $(^{87}Sr/^{86}Sr)_i$ increases from 0.7044 to 0.7055, reflecting progressive incorporation of ancient crustal components into the magma source from the early Late Cretaceous to the Paleocene. These findings indicate that the Qiuwo intrusions formed by partial melting of a juvenile basaltic lower crust, with increasing crustal contamination during ascent and emplacement. The temporal progression of magmatism—spanning the waning stages of Neo-Tethyan subduction to the initial India–Eurasia collision (~55 Ma)—supports a model in which slab breakoff and lithospheric delamination triggered decompression melting of the lower crust, while assimilation of older crustal materials intensified as the continental collision progressed. This work provides key geochemical evidence for the transition from arc to post-collisional magmatism in the western Gangdese belt and refines the timing and mechanism of crustal growth in southern Tibet.

Check for updates

Academic Editor: Alexey V. Ivanov

Received: 1 December 2025
Revised: 31 December 2025
Accepted: 5 January 2026
Published: 7 January 2026

Copyright: © 2026 by the authors. Licensee MDPI, Basel, Switzerland. This article is an open access article distributed under the terms and conditions of the Creative Commons Attribution (CC BY) license.

Keywords: intermediate to felsic intrusive rocks; geochronology; geochemical characteristics; geological implications; southern margin of the Lhasa terrane

1. Introduction

Granites are a significant component of the continental crust, and major granite plutons are predominantly found in subduction zones. They provide crucial insights into crustal growth and crust–mantle interactions [1,2]. The magmatic rocks in the Lhasa Terrane record the subduction of the Bangong–Nujiang Ocean and the Neo-Tethys Ocean, as well as the collision between the Indian and Eurasian continents [3,4]. As the region with the most developed magmatism in the Lhasa terrane, the widely distributed granites in the Gangdese provide valuable geological information for the study of the evolution of the Neo-Tethys Ocean [3,4]. Notably, Late Cretaceous to Paleocene magmatic activity constitutes a major part of the Gangdese plutonic system [5,6].

Late Cretaceous to Paleocene magmatic rocks in the southern margin of the Lhasa Terrane exhibit distinct characteristics of island arc magmatism [7–9]. Previous studies have suggested that the northward subduction of the Neo-Tethys Ocean led to intense magmatic activity during the Late Cretaceous to Paleocene in the southern margin of the Lhasa Terrane [10–13]. Zhu et al. [14] constrained the main collision time between the Indian and Eurasian continents to around 55 Ma. Therefore, the magmatic activity in the southern margin of the Lhasa Terrane during the Late Cretaceous to Paleocene may record the process from the late-stage subduction of the Neo-Tethys Ocean to the collision between the Indian and Eurasian continents. Although there have been numerous studies on the magmatic rocks of this period, the research intensity varies among different regions, with most studies focusing on the eastern segment. The western segment has fewer exposed intrusive rocks and is relatively less studied. In summary, multiple interpretations have been proposed for the deep geodynamic mechanisms governing the Late Cretaceous–Paleocene magmatism along the southern margin of the Lhasa terrane. These include roll-back of the subducted Neo-Tethyan oceanic slab [15–19], oceanic ridge subduction [20,21], normal-angle subduction from 100 to 85 Ma and subsequent low-angle or flat oceanic slab subduction from 85 to 80 Ma [22–24], partial melting of normal lower crust or fractional crystallization of more mafic magma from 95 to 86 Ma, partial melting of thickened lower crust from 85 to 73 Ma [25], roll-back or steepening of the subducted Neo-Tethyan slab [10,23], and lithospheric delamination after 68 Ma [24,25]. Overall, the genesis and geodynamic setting of the Late Cretaceous–Paleocene magmatic activity along the southern margin of the Lhasa Terrane remain contentious, underscoring the need for further detailed investigations.

This study conducted petrographic, zircon U-Pb dating, zircon Hf isotope, whole-rock major and trace element geochemical, and Sr-Nd isotope analyses on intermediate–acidic intrusive rocks in the Qiuwo area of the western segment of the southern margin of the Lhasa Terrane. The objectives were to determine the rock types and formation ages, reveal their petrogenesis, and explore the tectonic setting. This work aims to provide new evidence for the late-stage subduction evolution of the Neo-Tethys Ocean and the timing of the India-Eurasia continental collision.

2. Geological Background

The Lhasa Terrane is a colossal tectono-magmatic belt situated between the Bangong Lake–Nujiang Ocean suture zone and the Yarlung Zangbo suture zone. It extends in an east–west direction, bordered by the Himalayan terrane to the south and the Qiangtang terrane

to the north [26]. According to [8], the Lhasa Terrane is further subdivided into the North Lhasa sub-Terrane (NL), Central Lhasa sub-Terrane (CL), and South Lhasa sub-Terrane (SL) (Figure 1a). The study area is located in the Qiuwo area of Angren County, which is in the western segment of the southern Lhasa sub-terrane (Figure 1a). The South Lhasa sub-terrane is primarily composed of juvenile crust; however, the discovery of granites older than 496 Ma within this block by [27] suggests the possible presence of a Precambrian crystalline basement. The sub-terrane hosts Mesozoic to Cenozoic volcanic-sedimentary cover sequences, mainly distributed in its eastern part, including the Yeba Formation, the Sangri Group, and the Linzizong Group [28]. The Gangdese batholith, which constitutes the dominant component of the South Lhasa sub-terrane, formed from the Triassic to the Miocene. Together with the Linzizong volcanic rocks, it records the complete orogenic evolution of the region, encompassing the northward subduction of the Neo-Tethyan oceanic slab and subsequent India–Asia continental collision [3,4,6].

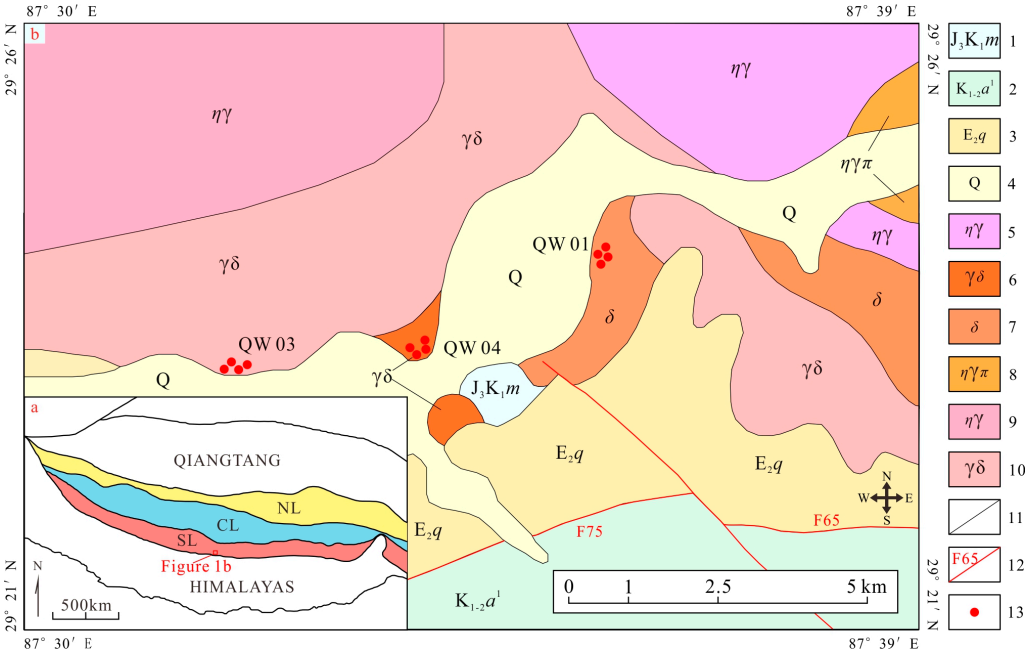


Figure 1. (**a**) Regional tectonic map of the Lhasa terrane (modified after [28]); (**b**) simplified geological map of the Late Cretaceous–Paleocene intermediate to felsic intrusive rocks in the Qiuwo area (modified after [29]). (NL—Northern Lhasa sub-Terrane; CL—Central Lhasa sub-Terrane; SL—Southern Lhasa sub-Terrane; 1. Mamuxia Formation; 2. Angren Formation; 3. Qiuwo Formation; 4. Quaternary; 5. Medium-grained hornblende monzogranite; 6. Early-stage medium to fine-grained granodiorite; 7. Medium- to fine-grained biotite hornblende diorite; 8. Medium- to coarse-grained porphyritic hornblende monzogranite; 9. Medium-grained biotite monzogranite; 10. Late-stage medium- to fine-grained granodiorite; 11. Geological boundary; 12. Fault; 13. Sampling locality).

The exposed strata in the study area are limited (Figure 1b) and, from oldest to youngest, include the Upper Jurassic–Lower Cretaceous Manuxia Formation, the Cretaceous Angren Formation, the Eocene Qiuwo Formation, and the Quaternary deposits. The Manuxia Formation (J_3k_1m) is only exposed in the southern part of the central region; the first member of the Angren Formation ($K_{1-2}a^1$) is distributed in an east–west belt in the southern part of the map area; the Qiuwo Formation (E_2q) is bounded by faults and distributed to the north of the first member of the Angren Formation; and the Quaternary deposits (Q) are deposited in an east–west belt along the river valley. Fold structures are not well developed in the study area, and faults are only present in the southern part [29]. Magmatic activity in the study area is frequent, and intermediate to acidic intrusive rocks are widely distributed. These include Late Cretaceous medium-grained hornblende mon-

zogranite, Late Cretaceous medium- to fine-grained granodiorite, Late Cretaceous medium- to fine-grained biotite-hornblende diorite, Late Cretaceous medium- to coarse-grained porphyritic hornblende monzogranite, Late Cretaceous medium-grained biotite monzogranite, and Paleocene medium- to fine-grained granodiorite (Figure 1b).

3. Sampling and Analytical Methods

3.1. Sample Characteristics

In this study, 12 samples of diorite and granodiorite rocks were collected from the Qiuwo area of Angren County. The granodiorites can be subdivided into two phases, with the late-stage granodiorite intruding and overlying the early-stage granodiorite. Sample locations are shown in Figure 1b.

The diorite was collected from the northeastern part of the study area. The weathered surface is light yellowish gray (Figure 2a,b), while the fresh surface is grayish white, with a massive structure and subhedral granular texture (Figure 2c). The main mineral composition includes plagioclase (about 65%), grayish white, vitreous luster, subhedral to euhedral elongated prismatic, first-order grayish white interference color, showing polysynthetic twinning; hornblende (about 20%), which is black with a metallic luster, mostly irregularly granular, and exhibits pale yellow-green to dark green pleochroism; biotite (about 5%), which is brown and transparent, flaky, with one set of perfect cleavage, and shows second- to third-order interference colors; quartz (about 5%), which has a conchoidal fracture, greasy luster, and appears subhedral to anhedral granular, being colorless and transparent under the microscope, with some parts being slightly turbid, and showing first-order grayish white to first-order yellowish white interference colors; and K-feldspar (about 4%), which is pinkish red, anhedral, filling the spaces between other minerals, colorless, with a turbid surface, and showing first-order grayish white interference colors, and exhibiting Carlsbad twinning. A small amount of accessory minerals (about 1%) are present, mainly zircon, titanite, and magnetite (Figure 3a–c).

The early granodiorite was collected from the central part of the study area. The weathered surface is light yellowish gray (Figure 2d,e), while the fresh surface is light gray, with a massive structure and subhedral granular texture (Figure 2f). The main mineral composition includes quartz (about 25%), which has a conchoidal fracture, greasy luster, anhedral granular, and is slightly turbid, with grain sizes ranging from about 0.1 to 3 mm, showing first-order grayish white to first-order yellowish white interference colors; plagioclase (about 40%), which is subhedral to euhedral elongated prismatic or granular, with grain sizes ranging from about 0.5 to 1 mm, showing first-order grayish white interference colors, and exhibiting polysynthetic twinning; K-feldspar (about 14%), which is pale pinkish red, anhedral granular, with a vitreous luster, colorless, and has a turbid surface, showing first-order grayish white interference colors, and exhibiting Carlsbad twinning; hornblende (about 15%), which is mostly irregularly granular, with grain sizes ranging from about 0.5 to 2 mm, showing pale yellow-green to dark green pleochroism, and exhibiting two sets of cleavage and simple twinning; biotite (about 5%), which is brown and transparent, flaky, with one set of perfect cleavage, and shows second- to third-order interference colors; and a small amount of accessory minerals (about 1%), mainly zircon, titanite, and magnetite (Figure 3d–f).

The late granodiorite was collected from the western part of the study area, where weathering and alteration are more intense. The weathered surface is yellow (Figure 2g,h), while the fresh surface is light gray, with a massive structure and subhedral to euhedral granular texture (Figure 2i). The main mineral composition includes quartz (about 20%), which has a conchoidal fracture, greasy luster, anhedral granular shape, and is slightly turbid, with grain sizes ranging from about 0.1 to 1 mm, showing first-order grayish white

to first-order yellowish white interference colors; plagioclase (about 45%), which is grayish white with a vitreous luster, subhedral to euhedral elongated prismatic, with grain sizes ranging from about 0.5 to 4 mm, showing first-order grayish white interference colors; K-feldspar (about 20%), which is pale pinkish red, anhedral granular, with a vitreous luster, colorless under the microscope, and has a turbid surface, showing first-order grayish white interference colors, and exhibiting Carlsbad twinning; hornblende (about 10%), which is black, mostly irregularly granular, with grain sizes ranging from about 0.5 to 2 mm, and exhibits pale yellow-green to dark green pleochroism, with two sets of cleavage; biotite (about 4%), black, platy, with a metallic luster, brown and transparent in plane-polarized light, with one set of perfect cleavage, and showing second- to third-order interference colors; and a small amount of accessory minerals (about 1%), mainly zircon, titanite, and magnetite (Figure 3g–i).

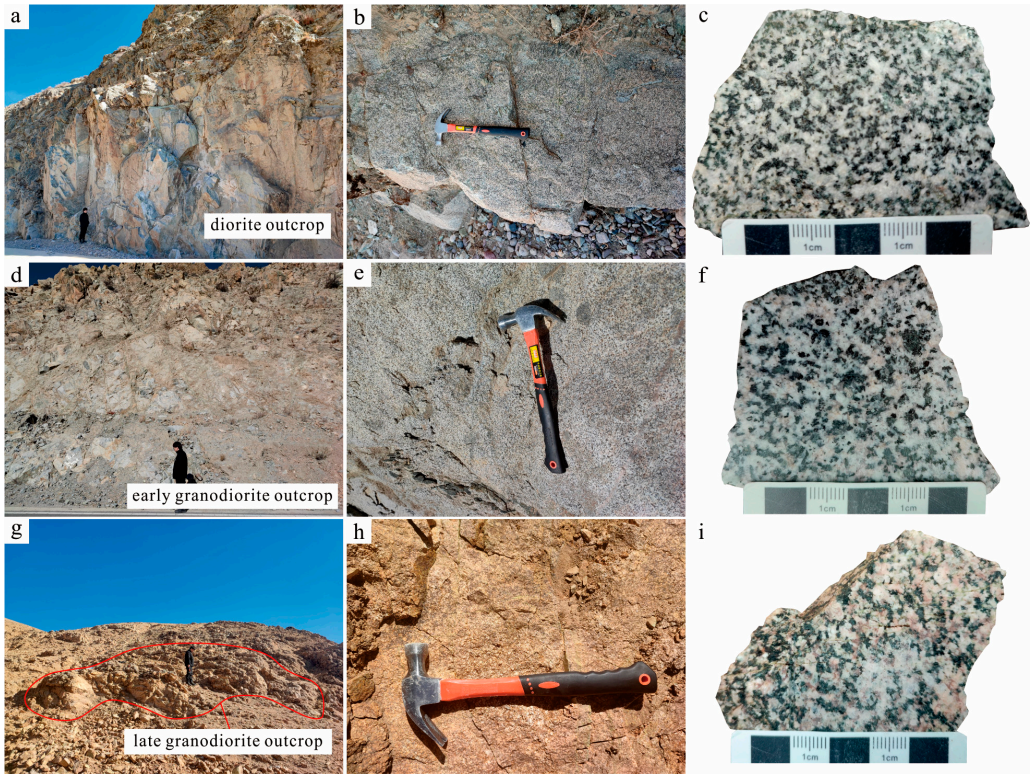


Figure 2. Field photographs and hand specimen images of intermediate to felsic intrusive rocks from the Qiuwo area, southern margin of the Lhasa terrane. ((**a**–**c**) show diorite, with (**a**) oriented toward the southwest; (**d**–**f**) show early-stage granodiorite, with (**d**) oriented toward the northeast; (**g**–**i**) show late-stage granodiorite, with (**g**) oriented toward the northeast).

3.2. Analytical Methods

First, a portion of the fresh samples was crushed and processed to separate pure zircon single minerals using heavy liquid separation. The separated zircons were then prepared as targets for analysis. LA-ICP-MS technology was used to obtain the U-Pb ages of the zircons, followed by in-situ Hf isotope analysis. Additionally, another part of the samples was ground into a 200-mesh powder for major and trace element geochemical and isotopic analyses.

The zircon LA-ICP-MS U-Pb geochronology tests were conducted at the State Key Laboratory of Geological Processes and Mineral Resources, China University of Geosciences (Beijing). The analysis was performed using a Thermo Fisher X-Series II quadrupole (Thermo Fisher Scientific, Waltham, MA, USA) inductively coupled plasma mass spectrometer, equipped with a GeoLas 193 excimer (Lambda Physik/Cymer LLC, San Diego,

CA, USA) solid-state laser ablation system from the United States. During the testing, the laser beam diameter for zircon ablation was 32 μm, with a frequency of 8 Hz and an energy density of approximately 2.5 J/cm^2. Helium was used as the carrier gas, and argon was used to adjust the sensitivity. The instrument was optimized using the NIST610 standard reference material from the United States. The external standard used was the 91500 zircon, and the monitoring sample was the GJ-1 zircon standard. The 91500 zircon standard was measured twice for every five sample points. The signal acquisition time for each sample point was 100 s, with the first 20 s dedicated to background signal collection and the next 50 s for sample signal collection. The offline data processing was carried out using ICPMSDataCal (version 10.8) [30]. The concordia diagrams and weighted mean age calculations were performed using Isoplot/Ex_ver3.

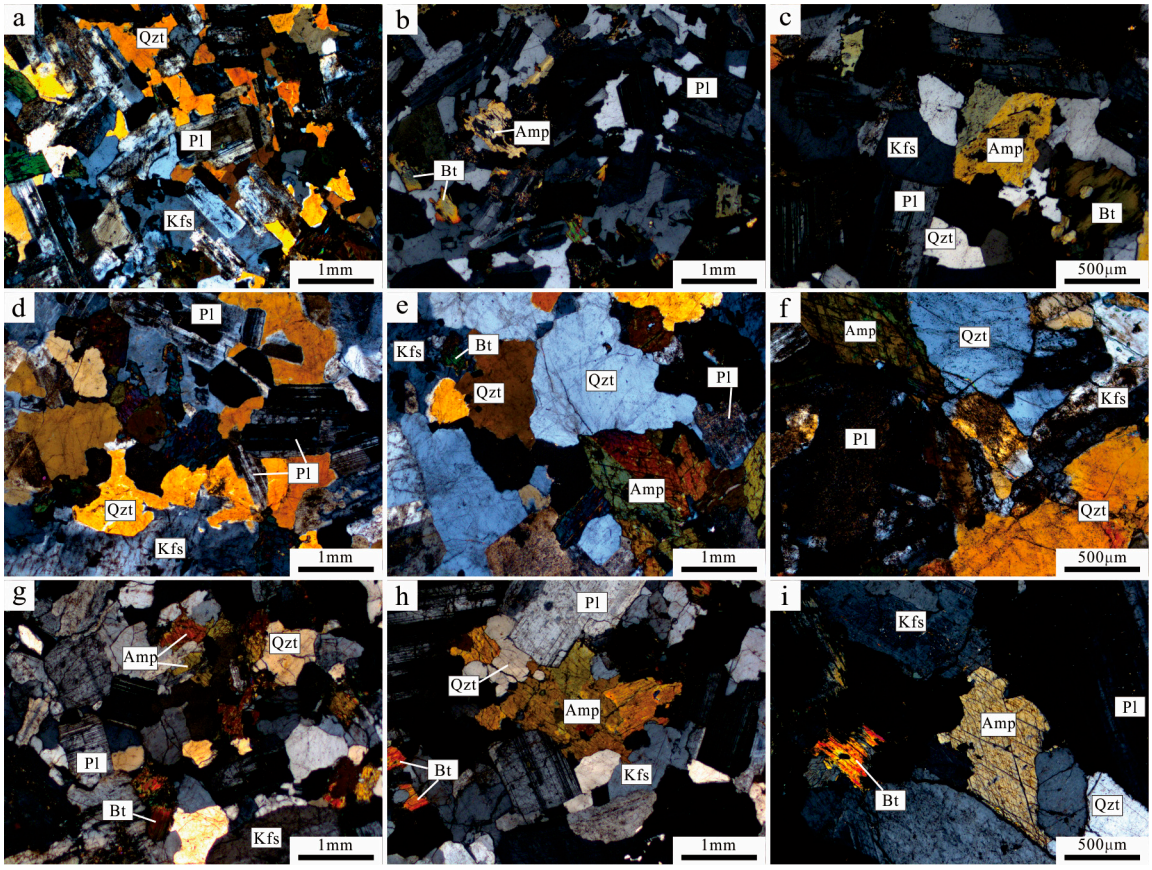


Figure 3. Photomicrographs of intermediate to felsic intrusive rocks from the Qiuwo area, southern margin of the Lhasa terrane ((**a**–**c**): diorite; (**d**–**f**): early-stage granodiorite; (**g**–**i**): late-stage granodiorite. Abbreviations: Qtz—quartz; Kfs—potassium feldspar; Pl—plagioclase; Bt—biotite; Amp—amphibole).

The zircon Lu-Hf isotope analysis was conducted at Nanjing Jupu Testing Technology Co., Ltd. (Nanjing, China). The Lu-Hf isotope measurement points were the same as those used for the zircon LA-ICP-MS U-Pb analysis. The instrument used was a Neptune multicollector ICP-MS (Thermo Fisher Scientific, Waltham, MA, USA) equipped with a GeoLas-193 laser (Lambda Physik/Cymer LLC, San Diego, CA, USA) ablation system. The laser beam diameter for analysis was 44 μm, with an ablation frequency of 8 Hz. High-purity helium was used as the carrier gas, and argon was used as the compensating gas, both of which were mixed uniformly before entering the ICP. Each measurement point included 30 s of background signal acquisition and 40 s of sample signal acquisition. After every five measurement points, the 91500, GJ-1, and Monastery standard zircons were

analyzed once. Detailed analytical procedures are described in Wu et al. [31]. The offline data processing was performed using the ICP-MS DataCal software [30].

The chemical pretreatment and mass spectrometry for whole-rock Sr-Nd isotope analysis were conducted at Nanjing Jupu Testing Technology Co., Ltd. The element concentrations in the processed sample solutions were accurately determined using an Agilent 7700x ICP-MS (Agilent Technologies, Santa Clara, CA, USA). After appropriate dilution, the Sr-Nd isotope ratios were measured using a Nu Plasma II MC-ICP-MS (Nu Instruments Ltd., Wrexham, UK). During the measurements, an internal correction of $^{86}Sr/^{88}Sr = 0.1194$ was used to correct for instrumental mass fractionation, and the international standard NIST SRM 987 was used as an external standard to correct for instrumental drift. For Nd isotopes, an internal correction of $^{146}Nd/^{144}Nd = 0.7219$ was applied, and the international standard JNdi-1 was used as an external standard to correct for instrumental drift. The U.S. Geological Survey (USGS) geochemical reference rock powders (e.g., basalt BCR-2, andesite AGV-2) were used as quality control blind samples. After chemical pretreatment and mass spectrometry, the isotope ratio results were within the error range and consistent with the reported values in the literature [32,33].

The major and trace element analyses of samples were conducted at Nanjing Jupu Testing Technology Co., Ltd. First, a portion of the whole-rock powder was dissolved in acid to prepare a solution. A part of this solution was appropriately diluted and introduced into an Agilent 5110 ICP-OES (Agilent Technologies, Santa Clara, CA, USA) in aerosol form to determine the major elements, excluding Si. Another portion of the whole-rock powder was subjected to alkaline digestion, and a part of the resulting solution was appropriately diluted and introduced into the Agilent 5110 ICP-OES to determine the Si content. Trace and rare earth element analyses were performed using inductively coupled plasma mass spectrometry (ICP-MS) on an Agilent 7700x ICP-MS. The finely ground samples were dissolved in acid to prepare solutions, which were then analyzed on the ICP-MS. For trace elements with concentrations greater than 50×10^{-6}, the deviation was less than 5%. For trace elements with concentrations between $(5\sim50) \times 10^{-6}$, the deviation was less than 10%. For trace elements with concentrations between $(0.5\sim5) \times 10^{-6}$, the deviation was less than 20%.

4. Results

4.1. Zircon Characteristics and U-Pb Geochronology

Cathodoluminescence (CL) images of zircons from three phases of intermediate to felsic intrusive rocks in the Qiuwo area at the southern margin of the Lhasa Terrane show that their grain sizes range from 100 to 200 μm, with well-preserved crystal forms and well-developed oscillatory zoning (Figure 4a,c,e). The Th/U values of the zircons (0.54~1.09) indicate that they are all magmatic zircons [34]. For the early granodiorite, 17 measurement points yielded $^{206}Pb/^{238}U$ ages ranging from 82.6 to 95.5 Ma, with a weighted mean age of 89.9 ± 0.75 Ma and an MSWD of 0.54 (Figure 4b, Supplementary Table S1). For the diorite, 22 measurement points yielded $^{206}Pb/^{238}U$ ages ranging from 62.6 to 82.6 Ma, with a weighted mean age of 68.6 ± 0.56 Ma and an MSWD of 0.41 (Figure 4d, Supplementary Table S1). For the late granodiorite, 17 measurement points yielded $^{206}Pb/^{238}U$ ages ranging from 53.0 to 61.0 Ma, with a weighted mean age of 56.75 ± 0.43 Ma and an MSWD of 1.6 (Figure 4f, Supplementary Table S1). The obtained ages accurately represent the crystallization times of these magmatic zircons.

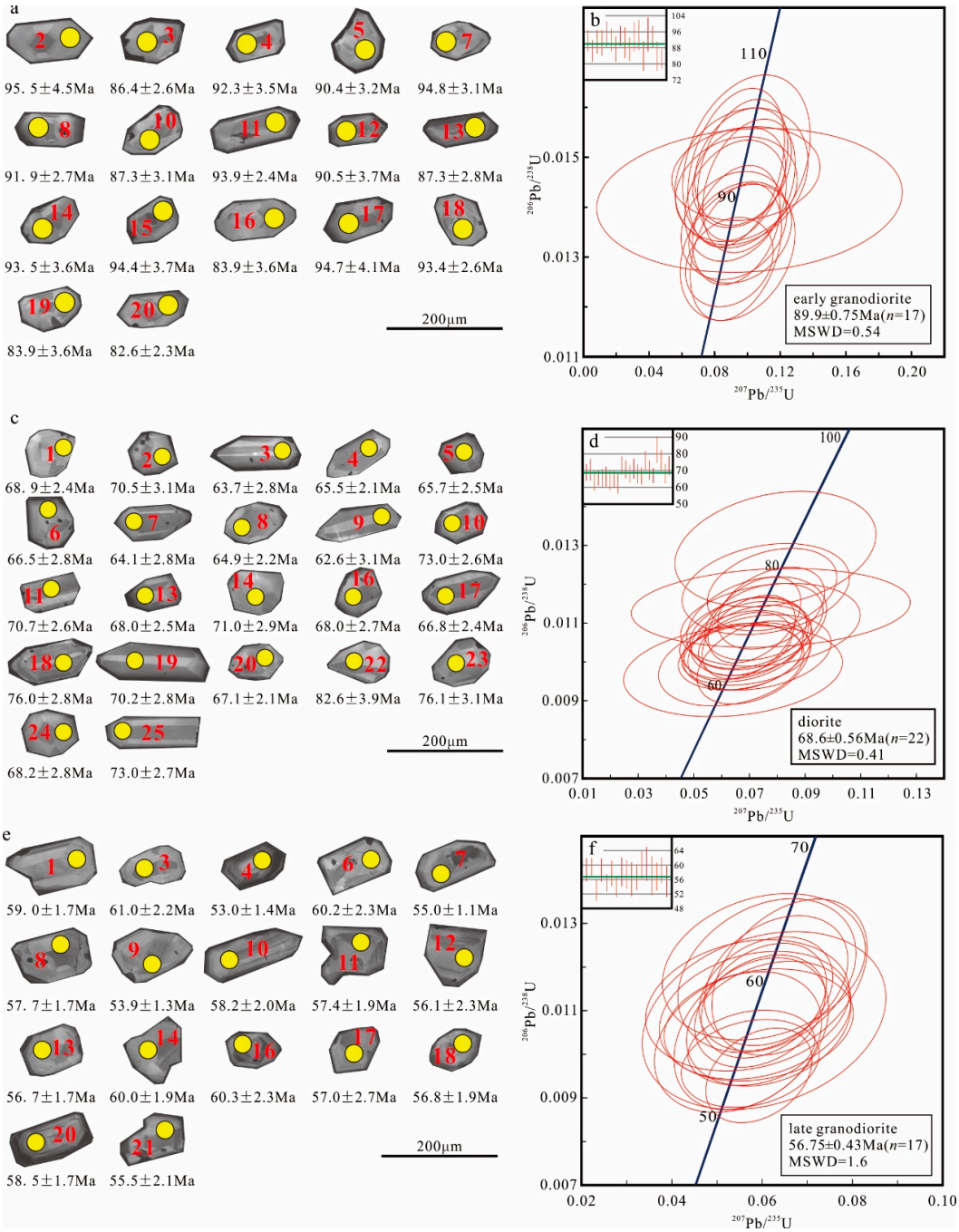


Figure 4. Cathodoluminescence (CL) images of zircons (**a**,**c**,**e**) and corresponding U-Pb concordia diagrams (**b**,**d**,**f**) for intermediate to felsic intrusive rocks from the Qiuwo area, southern margin of the Lhasa terrane.

4.2. Major and Trace Elements

According to Supplementary Table S2, the loss on ignition (LOI) of the 12 diorite and granodiorite samples ranges from 0.77% to 1.85%, all of which are less than 3%. This indicates that the geochemical data of the rocks are minimally affected by alteration and can be used to discuss the petrogenesis of the rocks.

Late Cretaceous granodiorite: The SiO_2 content ranges from 62.35% to 64.65% (average 63.80%); Al_2O_3 content ranges from 15.86% to 16.17% (average 16.03%); MgO content ranges from 2.06% to 2.38% (average 2.22%); Na_2O content ranges from 3.66% to 3.97% (average 3.76%); and K_2O content ranges from 2.06% to 2.60% (average 2.42%) (Supplementary Table S2). In the SiO_2-K_2O + Na_2O diagram (Figure 5a), the samples fall

within the granodiorite field. In the SiO_2-K_2O diagram (Figure 5b), the samples are located in the calc-alkaline and high-K calc-alkaline series fields. The A/CNK values range from 0.92 to 0.97 (average 0.94), and in the A/CNK-A/NK diagram (Figure 5c), the samples are situated in the metaluminous field. The spider diagram of trace elements (Figure 6a) shows that the Late Cretaceous granodiorite is enriched in the large-ion lithophile element (LILE) K, and relatively depleted in the high-field-strength elements (HFSEs) U, Nb, Ta, P, and Ti, while Zr and Hf are relatively enriched. The ΣREE for the Late Cretaceous granodiorite ranges from (81.01~136.24) $\times 10^{-6}$ (average 98.97 $\times 10^{-6}$); ΣLREE is relatively enriched, while ΣHREE is relatively depleted (Figure 6b). The ΣLREE/ΣHREE ratio ranges from 8.39 to 11.42 (average 9.23). The $(La/Yb)_N$ values range from 10.26 to 15.78 (average 11.84). The δEu values range from 0.78 to 0.88 (average 0.84), indicating a negative Eu anomaly. The δCe values range from 1.02 to 1.03 (average 1.02). The Sr/Y ratios range from 34.51 to 45.16 (average 38.55).

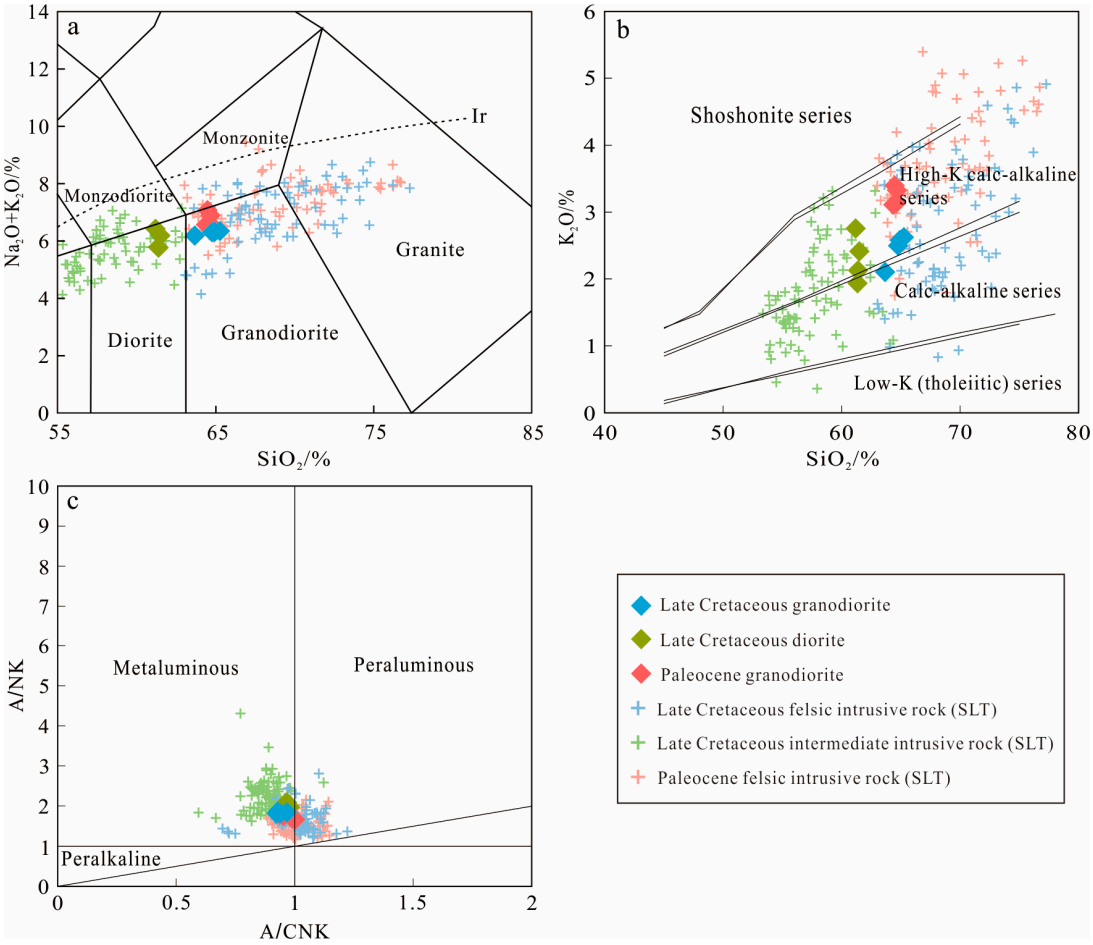


Figure 5. Geochemical classification diagrams for intermediate to felsic intrusive rocks from the Qiuwo area, southern margin of the Lhasa terrane: (**a**) total alkali-SiO_2 diagram (base map after [35]); (**b**) K_2O-SiO_2 diagram (base map after [36]); (**c**) A/NK-A/CNK diagram (base map after [37]). (Late Cretaceous felsic intrusive rock data are from [8,16–19,21,23–25,38–40]. Late Cretaceous intermediate intrusive rock data are from [8,18,19,21,25,39–43]. Paleocene felsic intrusive rock data are from [18,25,40,42,44–51]).

Late Cretaceous diorite: The SiO_2 content ranges from 59.53% to 60.46% (average 60.03%); Al_2O_3 content ranges from 16.78% to 17.22% (average 16.94%); MgO content ranges from 2.42% to 2.65% (average 2.57%); Na_2O content ranges from 3.53% to 3.76% (average 3.62%); and K_2O content ranges from 1.91% to 2.68% (average 2.26%) (Supplementary Table S2). In the SiO_2-K_2O + Na_2O diagram (Figure 5a), the samples fall

within the diorite field. In the SiO_2-K_2O diagram (Figure 5b), the samples are located in the calc-alkaline and high-K calc-alkaline series fields. The A/CNK values range from 0.95 to 0.98 (average 0.96), and in the A/CNK-A/NK diagram (Figure 5c), most of the samples are situated in the metaluminous field, with only one sample located at the boundary between the metaluminous and peraluminous fields. The spider diagram of trace elements (Figure 6a) shows that the Late Cretaceous diorite is enriched in the large-ion lithophile elements (LILEs) K and Th, and relatively depleted in the high-field-strength elements (HFSEs) U, Nb, Ta, P, and Ti, while Zr and Hf are relatively enriched. The ΣREE for the Late Cretaceous diorite ranges from (105.03~110.14) × 10^{-6} (average 107.36 × 10^{-6}); ΣLREE is relatively enriched, while ΣHREE is relatively depleted (Figure 6b). The ΣLREE/ΣHREE ratio ranges from 8.03 to 9.18 (average 8.49). The $(La/Yb)_N$ values range from 9.34 to 10.69 (average 9.80). The δEu values range from 0.83 to 0.89 (average 0.86), indicating a negative Eu anomaly. The δCe values range from 1.01 to 1.02 (average 1.01). The Sr/Y ratios range from 27.18 to 32.86 (average 29.68).

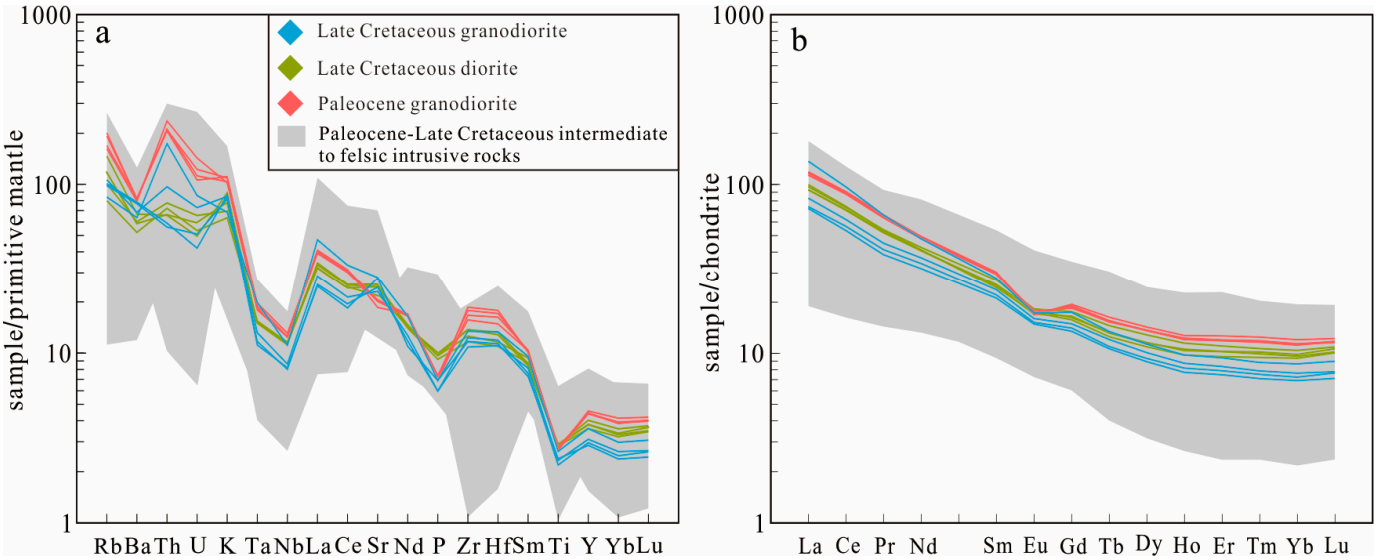


Figure 6. Primitive mantle-normalized trace element spider diagrams (**a**) and chondrite-normalized rare earth element (REE) patterns (**b**) for intermediate to felsic intrusive rocks from the Qiuwo area, southern margin of the Lhasa terrane. (The primitive mantle and chondrite normalization values are from [52]. The data are sourced from [24]).

Paleocene granodiorite: The SiO_2 content ranges from 63.21% to 64.33% (average 63.70%); Al_2O_3 content ranges from 15.60% to 15.76% (average 15.71%); MgO content ranges from 2.12% to 2.24% (average 2.16%); Na_2O content ranges from 3.38% to 3.58% (average 3.47%); and K_2O content ranges from 3.07% to 3.33% (average 3.20%) (Supplementary Table S2). In the SiO_2-K_2O + Na_2O diagram (Figure 5a), the samples fall within the granodiorite field. In the SiO_2-K_2O diagram (Figure 5b), the samples are located in the high-K calc-alkaline series field. The A/CNK values range from 0.94 to 1.00 (average 0.97), and in the A/CNK-A/NK diagram (Figure 5c), the samples are situated in the metaluminous field. The spider diagram of trace elements (Figure 6a) shows that the Paleocene granodiorite is significantly enriched in the large-ion lithophile elements (LILEs) K and Th, and relatively depleted in the high-field-strength elements (HFSEs) U, Nb, Ta, Sr, P, and Ti, while Zr and Hf are relatively enriched. The ΣREE for the Paleocene granodiorite ranges from (127.26~132.16) × 10^{-6} (average 129.83 × 10^{-6}); ΣLREE is relatively enriched, while ΣHREE is relatively depleted (Figure 6b). The ΣLREE/ΣHREE ratio ranges from 8.66 to 8.97 (average 8.84). The $(La/Yb)_N$ values range from 9.90 to 10.40 (average 10.16). The δEu values range from 0.70 to 0.76 (average 0.72), indicating a negative Eu anomaly. The δCe

values range from 1.02 to 1.03 (average 1.03). The Sr/Y ratios range from 18.88 to 21.67 (average 20.74).

4.3. Zircon Lu-Hf Isotopes

Seven zircon grains were selected from the Late Cretaceous granodiorite and underwent U-Pb dating for further analysis and testing. The $^{176}Hf/^{177}Hf$ ratios range from 0.000623 to 0.001028, and the $^{176}Hf/^{177}Hf$ ratios range from 0.283001 to 0.283021. The $(^{176}Hf/^{177}Hf)_i$ values range from 0.282999 to 0.283019. The $\varepsilon_{Hf}(t)$ values range from +10.03 to +10.78 (average +10.40). The T_{DM} values range from 356 to 327 Ma, and the T_{2DM} values range from 513 to 466 Ma (Supplementary Table S3).

Nine zircon grains were selected from the Late Cretaceous diorite and underwent U-Pb dating for further analysis and testing. The $^{176}Lu/^{177}Hf$ ratios range from 0.001069 to 0.001713, and the $^{176}Lu/^{177}Hf$ ratios range from 0.282901 to 0.282972. The $(^{176}Hf/^{177}Hf)_i$ values range from 0.282900 to 0.282970. The $\varepsilon_{Hf}(t)$ values range from +5.93 to +8.43 (average +7.54). The T_{DM} values range from 498 to 399 Ma, and the T_{2DM} values range from 755 to 595 Ma (see Supplementary Table S3).

Ten zircon grains were selected from the Paleocene granodiorite and underwent U-Pb dating for further analysis and testing. The $^{176}Hf/^{177}Hf$ ratios range from 0.000591 to 0.001769, and the $^{176}Hf/^{177}Hf$ ratios range from 0.282851 to 0.282903. The $(^{176}Hf/^{177}Hf)_i$ range from 0.282850 to 0.282902. The $\varepsilon_{Hf}(t)$ values range from +4.02 to +5.90, with an average of +4.91. The T_{DM} model ages range from 569 to 491 Ma, and the T_{2DM} model ages range from 872 to 753 Ma (Supplementary Table S3).

4.4. Sr-Nd Isotopes

The Late Cretaceous granodiorite exhibits initial $^{87}Sr/^{86}Sr$ ratios ranging from 0.326741 to 0.326742 with corresponding $^{87}Rb/^{86}Sr$ ratios of 0.704824–0.704840. For Nd isotopes, the samples yield $^{143}Nd/^{144}Nd$ values between 0.512731 and 0.512739 and a $^{147}Sm/^{144}Nd$ ratio of 0.124284. Calculations show that the $(^{87}Sr/^{86}Sr)_i$ values for the Late Cretaceous granodiorite range from 0.704406 to 0.704423, and the $(^{143}Nd/^{144}Nd)_i$ values range from 0.512658 to 0.512666. The $\varepsilon_{Nd}(t)$ values are between 2.65 and 2.81. The first-order model age values are concentrated between 717.17 and 703.20 Ma, while the second-order model ages are concentrated between 676.01 and 662.96 Ma (Supplementary Table S4).

The Late Cretaceous diorite exhibits initial $^{87}Sr/^{86}Sr$ ratios of 0.388053–0.388059, with corresponding $^{87}Rb/^{86}Sr$ ratios ranging from 0.705231 to 0.705395. Its $^{143}Nd/^{144}Nd$ ratios vary between 0.512658 and 0.512672, and the associated $^{147}Sm/^{144}Nd$ ratio is 0.122408. Calculations show that the $(^{87}Sr/^{86}Sr)_i$ values for the Late Cretaceous diorite range from 0.704856 to 0.705019, and the $(^{143}Nd/^{144}Nd)_i$ values range from 0.512603 to 0.512617. The $\varepsilon_{Nd}(t)$ values are between 1.04 and 1.31. The first-order model age values are concentrated between 824.41 and 801.23 Ma, while the second-order model ages are concentrated between 789.62 and 767.50 Ma (Supplementary Table S4).

The Paleocene granodiorite displays initial $^{87}Sr/^{86}Sr$ ratios ranging from 0.791965 to 0.791966, corresponding to $^{87}Rb/^{86}Sr$ ratios of 0.706099–0.706109. For Nd isotopes, the samples yield $^{143}Nd/^{144}Nd$ values between 0.512588 and 0.512605, with a $^{147}Sm/^{144}Nd$ ratio of 0.121383. Calculations show that the $(^{87}Sr/^{86}Sr)_i$ values for the Paleocene granodiorite range from 0.705460 to 0.705469, and the $(^{143}Nd/^{144}Nd)_i$ values range from 0.512543 to 0.512560. The $\varepsilon_{Nd}(t)$ values are between -0.43 and -0.11. The first-order model age values are concentrated between 930.35 and 903.32 Ma, while the second-order model ages are concentrated between 899.52 and 873.44 Ma (Supplementary Table S4).

5. Discussion

5.1. Chronology

The Cretaceous granites along the southern margin of the Lhasa Terrane are among the earliest recognized and studied magmatic rocks in this region. Schärer et al. [53] reported a Late Cretaceous diorite near Dazhuka with an age of approximately 94 Ma. Subsequently, contemporaneous granite bodies have been found in multiple areas along the southern margin of the Lhasa Terrane [9,20,25]. The rocks formed during the early Late Cretaceous (95~86 Ma) along the southern margin of the Lhasa Terrane are mainly intermediate to mafic [15–17,20,39], while those formed during the late Late Cretaceous (87~73 Ma) are predominantly granitic [9,22].

The Paleocene–Eocene period was the most active period of magmatic activity along the southern margin of the Lhasa Terrane. There was a significant magmatic eruption around 50 Ma [9,54,55]. The granites formed during this period constitute the main body of the Gangdese batholith, which is widely distributed and has a complex magmatic composition. A typical example is the Qushui batholith [9,11,56]. During the same period, frequent magmatic activity along the southern margin of the Lhasa Terrane also formed the Linzizong volcanic rocks, which form the largest volcanic rock belt on the Tibetan Plateau.

The intermediate to felsic intrusive rocks can be divided into three phases (Figure 7a). The early granodiorite formed during the Late Cretaceous (89.9 ± 0.75 Ma); the diorite formed during the Late Cretaceous (68.6 ± 0.56 Ma); and the late granodiorite formed during the Paleocene (56.75 ± 0.43 Ma). Based on a synthesis of previous studies, the Late Cretaceous to early Eocene magmatic activity along the southern margin of the Lhasa terrane can be categorized into four distinct stages according to the peaks in zircon U-Pb age spectra. The first stage, from 100 to 86 Ma, is mainly distributed in areas such as Milin, Lilong, Nuri, Dazhuka, Nimu, and Nanmuling. The second stage, from 85 to 74 Ma, is primarily found in Milin, Langxian, Zedang, and Lilong. The third stage, from 68 to 55 Ma, is mainly distributed in Linzhi, Riduo, and Xietongmen. The fourth stage, after 55 Ma, is characterized by exceptionally active magmatic activity with a wide distribution (Figure 7b).

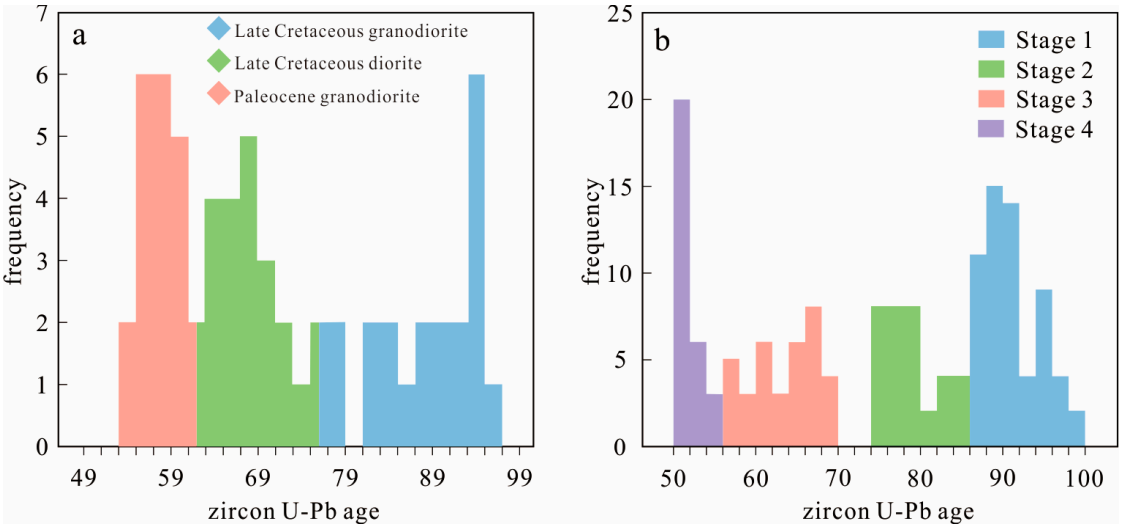


Figure 7. (**a**) Histogram of single zircon U–Pb ages for intermediate to felsic intrusive rocks from the Qiuwo area, southern margin of the Lhasa terrane; (**b**) the age distribution of Late Cretaceous to early Eocene magmatism along the southern margin of the Lhasa terrane (the data are sourced from [24]).

5.2. Rock Genesis

5.2.1. Rock Types of the Three Pluton Phases

The intermediate to felsic intrusive rocks in the Qiuwo area have w(Na2O) > 3.2% and contain amphibole, which are consistent with the characteristics of I-type granitic rocks [57]. In the Zr + Nb + Ce + Y-FeO^T/MgO, Zr + Nb + Ce + Y-(K_2O + Na_2O)/CaO, SiO_2-Ce, K_2O-Na_2O diagrams (Figure 8), all three phases of the intrusive rocks fall within the I-type granitic rock field. Additionally, the zircon saturation temperature of the granite melt can be estimated using the Zr content and major element compositions. The formula proposed by Watson and Harrison [58] is as follows:

$$T(°C) = 12{,}900/[0.85M + \ln(DZr) + 2.95] - 273.15 \quad (1)$$

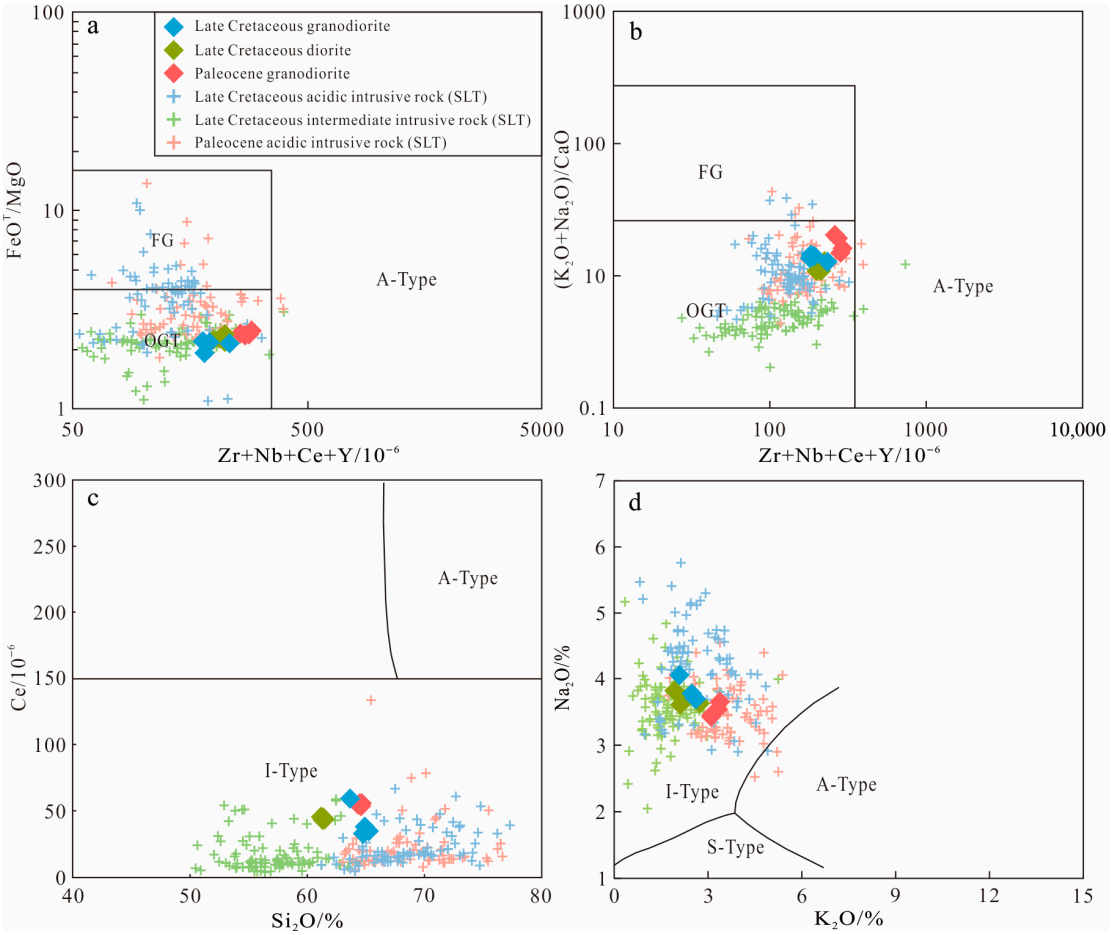


Figure 8. Discrimination diagrams for granitoid rocks: (**a**) Zr + Nb + Ce + Y-FeOT/MgO (base diagram after [59]); (**b**) Zr + Nb + Ce + Y-(K_2O + Na_2O)/CaO (base diagram after [59]); (**c**) SiO_2-Ce (base diagram after [59]); (**d**) K_2O-Na_2O (base diagram after [60]). (FG—Fractionated granites; OGT—Unfractionated I-type, M-type and S-type granites. The data are sourced from [24]).

Let Si + Ca + Na + Al + K + Mg + Fe + P = 1 (in molar amounts). In this equation: DZr = 49600/Zr content in the melt, and M = (Na + 2Ca + K)/(Si × Al) in molar amounts. The calculated zircon saturation temperatures are as follows: for the Late Cretaceous granodiorite, the temperatures range from 737.03 to 752.01 °C, with an average of 746.65 °C; for the Late Cretaceous diorite, the temperatures range from 741.23 to 756.70 °C, with an average of 749.06 °C; and for the Paleocene granodiorite, the temperatures range from 776.12 to 785.50 °C, with an average of 780.27 °C. These temperatures are all close to the initial crystallization temperatures of I-type granitic rocks (750–850 °C) [58]. In the

Zr + Nb + Ce + Y-FeO^T/MgO and Zr + Nb + Ce + Y-(K_2O + Na_2O)/CaO diagrams (Figure 8a,b), all three phases of the intrusive rocks fall within the undifferentiated granite field. Therefore, the three phases of intermediate to felsic intrusive rocks in the Qiuwo area are all undifferentiated I-type granitic rocks.

5.2.2. Magma Source and Petrogenesis

The genesis of I-type granitic rocks can be divided into three mechanisms: (1) differentiation of mantle-derived magmas [61,62]; (2) mixing of crustal and mantle magmas [63,64]; and (3) partial melting of crustal materials [65,66].

The Hf isotopic characteristics of magmatic zircons are effective indicators for identifying magmas from different source regions, as zircons from different source regions have distinct Hf isotopic compositions. Specifically, positive to near-zero $\varepsilon_{Hf}(t)$ values reflect a source derived from the depleted mantle and/or juvenile crust (newly extracted from the mantle), whereas negative $\varepsilon_{Hf}(t)$ values point to the involvement of ancient crustal materials [31]. In the Qiuwo area, the $\varepsilon_{Hf}(t)$ values for the Late Cretaceous granodiorite range from +10.03 to +10.78 (average +10.40); for the Late Cretaceous diorite, the $\varepsilon_{Hf}(t)$ values range from +5.93 to +8.43 (average +7.54); and for the Paleocene granodiorite, the $\varepsilon_{Hf}(t)$ values range from +4.02 to +5.90 (average +4.91). The positive $\varepsilon_{Hf}(t)$ values indicate that the source rocks for all three phases of the intrusive rocks are juvenile basaltic lower crustal rocks (Figure 9).

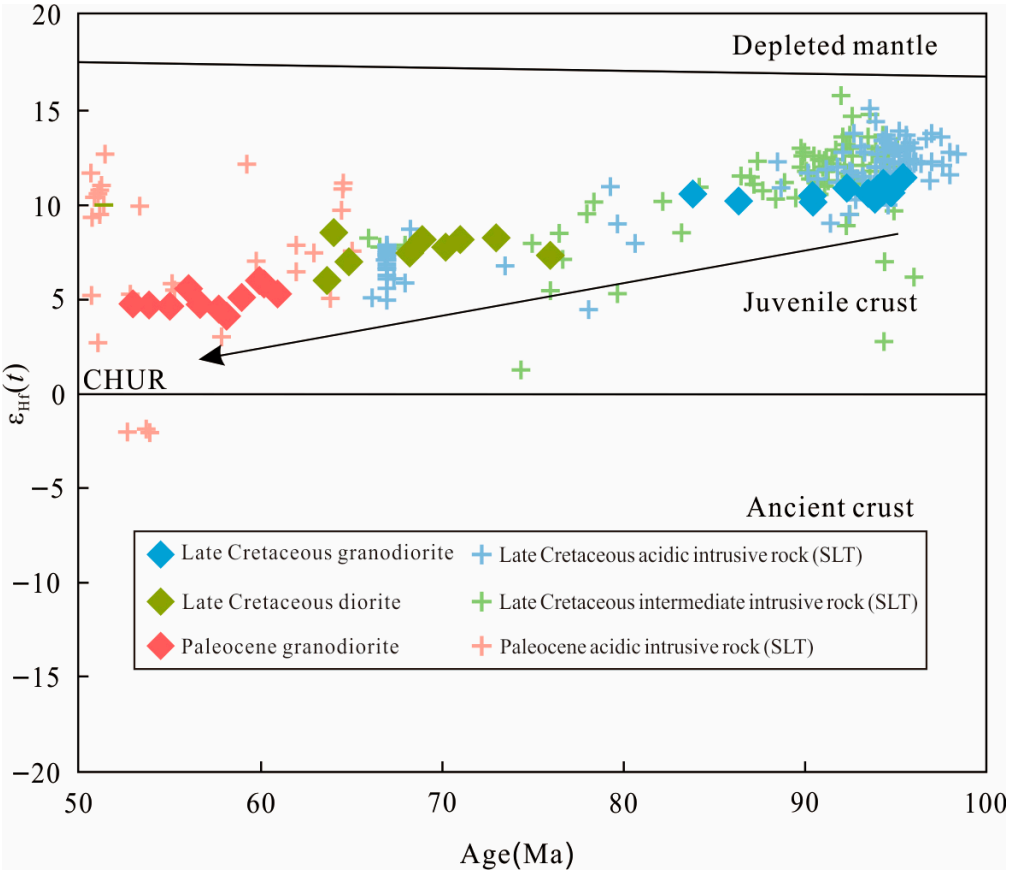


Figure 9. Zircon U-Pb age-$\varepsilon_{Hf}(t)$ diagram for intermediate to felsic intrusive rocks from the Qiuwo area, southern margin of the Lhasa terrane. (The data for Late Cretaceous felsic intrusive rocks are from [7,8,18,21,25,39]; the data for Late Cretaceous intermediate intrusive rocks are from [7,8,15,18,19,39,41,67]; the data for Paleocene felsic intrusive rocks are from [25,44–46,48–51,68]).

Additionally, Sr-Nd isotopes can also be used to investigate the source of materials [69]. In general, negative εNd(t) values indicate that the magma was derived from ancient crustal sources, whereas positive εNd(t) values suggest an origin from juvenile crustal materials or a depleted mantle reservoir. Furthermore, granites originating from juvenile crust or the depleted mantle are typically characterized by low initial $^{87}Sr/^{86}Sr$ ratios ($(^{87}Sr/^{86}Sr)_i$) [70,71]. In the Qiuwo area, the $\varepsilon_{Nd}(t)$ values for the Late Cretaceous granodiorite range from 2.65 to 2.81, with $(^{87}Sr/^{86}Sr)_i$ values ranging from 0.704406 to 0.704423. The Late Cretaceous diorite has $\varepsilon_{Nd}(t)$ values ranging from 1.04 to 1.31, with $(^{87}Sr/^{86}Sr)_i$ values ranging from 0.704856 to 0.705019. Both phases of these rocks exhibit characteristics of juvenile crust or depleted mantle. The Paleocene granodiorite has $\varepsilon_{Nd}(t)$ values ranging from −0.43 to −0.11 and $(^{87}Sr/^{86}Sr)_i$ values ranging from 0.705460 to 0.705469, indicating that it is derived from ancient crust, which does not align with the previous analysis suggesting that its source rock is juvenile basaltic lower crust. Generally, the Sr-Nd isotopic characteristics of magmas can be influenced by crustal contamination during their ascent. The decoupling of Sr-Nd isotopes and Hf isotopes indicates that a significant amount of ancient crustal material was incorporated into the Paleocene granodiorite during its formation. From the $(^{87}Sr/^{86}Sr)_i$-$\varepsilon_{Nd}(t)$ diagram (Figure 10), it can be seen that the three phases of intrusive rocks in the Qiuwo area, from the early Late Cretaceous to the Paleocene, show a continuous decrease in $\varepsilon_{Nd}(t)$ values and a continuous increase in $(^{87}Sr/^{86}Sr)_i$ values as they become younger. This trend is also evident in the zircon age-$\varepsilon_{Hf}(t)$ diagram (Figure 9), where younger magmatic zircons have lower $\varepsilon_{Hf}(t)$ values. The trends in Sr-Nd isotopes and zircon Hf isotopes both indicate that from the early Late Cretaceous to the Paleocene, an increasing amount of ancient crustal material was incorporated into the magmas.

In the La-La/Sm and La-La/Yb diagrams, samples from the three intrusive phases in the Qiuwo area define a coherent linear trend with a positive slope, indicating that the formation of all three phases is closely related to partial melting [72] (Figure 11). The δEu values of the three phases of intermediate to felsic intrusive rocks in the Qiuwo area are all less than 1, with negative Eu anomalies indicating that plagioclase fractionation occurred to some extent during the rock-forming process [73].

In summary, the parental magmas of the intermediate to felsic intrusive rocks in the Qiuwo area of the southern margin of the Lhasa terrane formed from the partial melting of wedge-shaped mantle peridotites. These magma melts, due to their lower density, migrated upward to the crust–mantle boundary where they cooled and formed a new basaltic lower crust [74]. Subsequently, these newly formed basaltic lower crustal rocks underwent partial melting and were variably contaminated by ancient crustal materials before intruding into the crust, forming the three phases of intermediate to felsic intrusive rocks in the Qiuwo area. During the intrusion process, the magmas experienced a certain degree of fractional crystallization.

5.3. Tectonic Setting and Petrogenesis Dynamics Mechanisms

The petrogeochemical data of the intermediate to felsic intrusive rocks in the Qiuwo area and the collected data from coeval intrusive rocks in the southern margin of the Lhasa terrane show that these rocks are generally enriched in ΣLREE and LILE, and relatively depleted in ΣHREE and HFSE, with high Al_2O_3 and low TiO_2 contents. In the Y-Nb, Y + Nb-Rb, and Yb + Ta-Rb diagrams (Figure 12) [75], the three phases of intrusive rocks and the collected data almost all fall within the volcanic arc granite field, indicating that these three phases of intrusive rocks formed in a subduction tectonic setting.

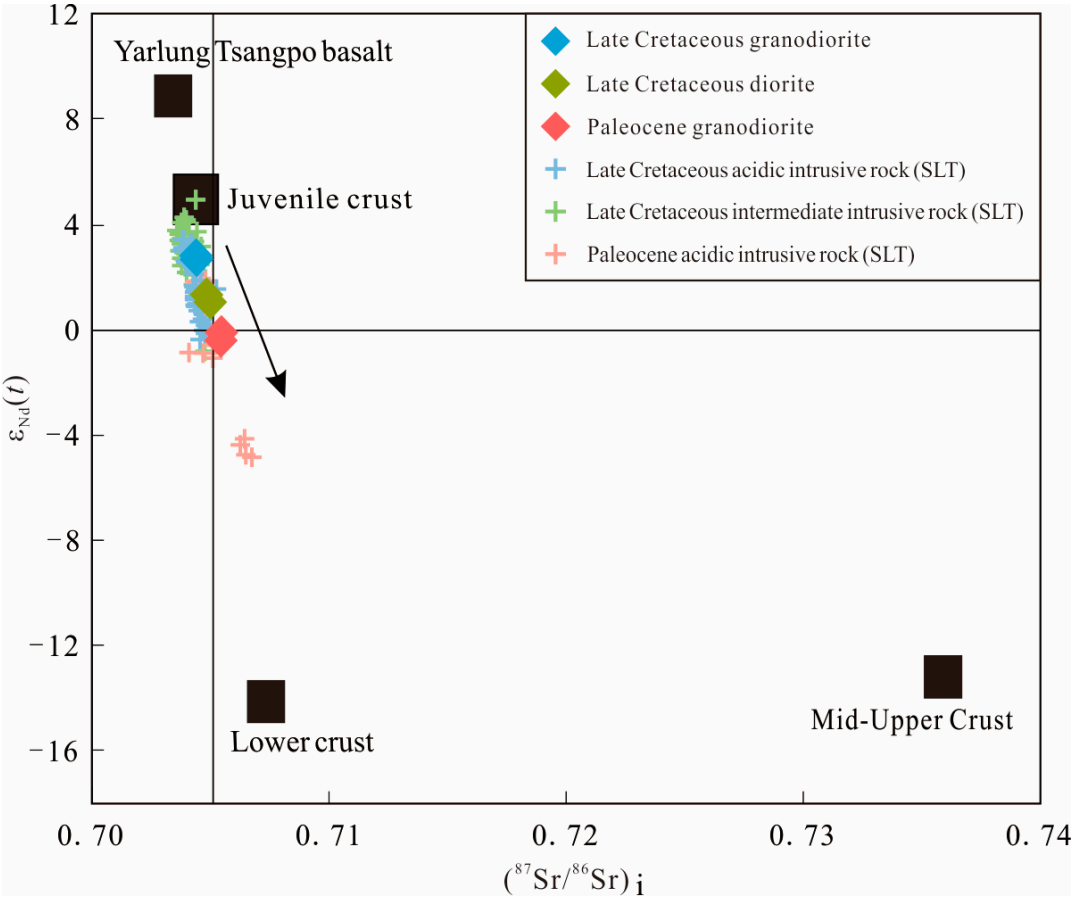


Figure 10. Initial $(^{87}Sr/^{86}Sr)_i$-$\varepsilon_{Nd}(t)$ diagram for intermediate to felsic intrusive rocks from the Qiuwo area along the southern margin of the Lhasa terrane. (Data for Late Cretaceous felsic intrusive rocks are cited from [16,18,39,40]. Data for Late Cretaceous intermediate intrusive rocks are cited from [15,16,18,19,39–41]. Data for Paleocene felsic intrusive rocks are cited from [18,40,44,47]).

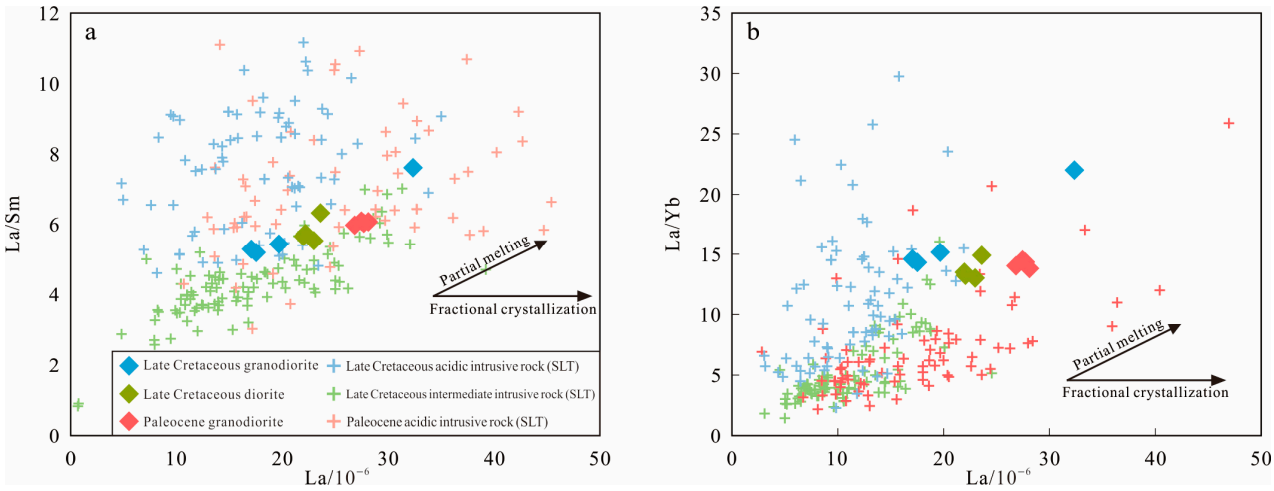


Figure 11. La-La/Sm (**a**) and La-La/Yb (**b**) diagrams for intermediate to felsic intrusive rocks from the Qiuwo area along the southern margin of the Lhasa terrane. (Late Cretaceous felsic intrusive rock data are from [8,16–19,21,23–25,38–40]. Late Cretaceous intermediate intrusive rock data are from [8,18,19,21,25,39–43]. Paleocene felsic intrusive rock data are from [18,25,40,42,44–51]).

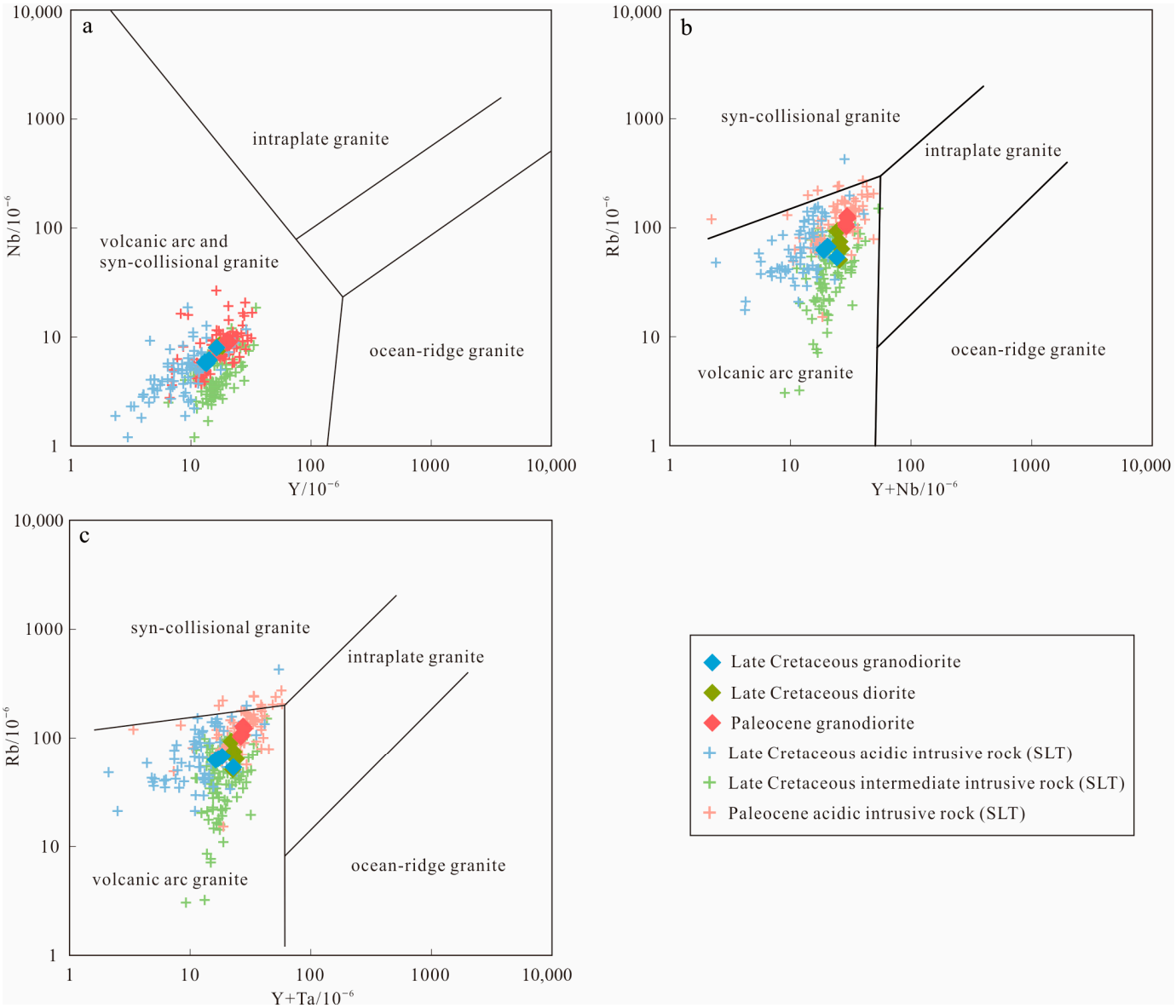


Figure 12. Tectonic discrimination diagrams for intermediate to felsic intrusive rocks from the Qiuwo area along the southern margin of the Lhasa terrane, based on (**a**) Y-Nb, (**b**) Y + Nb-Rb, and (**c**) Yb + Ta-Rb. (Baseline fields after [75]. The data are sourced from [24]).

Before the collision between the Indian and Eurasian plates, there were two periods of magmatic "flare-up" events in the southern margin of the Lhasa terrane during the Early to Middle Jurassic and Late Cretaceous [8,15,23,76,77]. The formation age of the Late Cretaceous granodiorite in the Qiuwo area of the southern margin of the Lhasa terrane falls within the period of the Late Cretaceous magmatic "flare-up" (Figure 7b, Stage 1). The dynamic mechanism for this period of magmatic "flare-up" remains inconclusive. Some scholars attribute the dynamic background of this magmatic "flare-up" to the subduction of the Neo-Tethys Ocean spreading ridge [20,21,78], while others suggest it is related to the rollback of the subducting Neo-Tethys Ocean slab [15,23,39].

The subduction of a spreading ridge is a crucial stage in the process of ocean closure. Cole and Stewart [79] proposed that the gradual subduction of a mid-ocean ridge would lead to progressively younger magmatic activity along the subduction zone due to the angle between the spreading ridge and the subduction zone. However, studies have shown that there is no such trend in the magmatic activity between 95~85 Ma in the southern

margin of the Lhasa terrane [80]. Therefore, the Late Cretaceous magmatic "flare-up" in the Gangdese arc was not caused by the subduction of a spreading ridge.

Slab rollback can also lead to magmatic "flare-ups" [5,81]. When the subduction angle changes from low to high, arc magmatism migrates towards the trench, and this process can cause upwelling of asthenospheric mantle material, resulting in a magmatic "flare-up" [81]. After the magmatic flare-up event during the Early to Middle Jurassic, the southern margin of the Lhasa terrane entered a magmatic hiatus [8,23,68,82]. During this hiatus, a large number of magmatic rocks dated at 125–110 Ma developed in the central Lhasa terrane and the northern margin. Around 96–86 Ma, frequent magmatic activity reappeared in the southern margin of the Lhasa terrane [15]. The spatiotemporal patterns of magmatic activity in the Lhasa terrane from the Early Jurassic to the Late Cretaceous suggest that the Neo-Tethys Ocean plate was subducting at a low angle during the Early Cretaceous. After the magmatic hiatus, the rollback of the Neo-Tethys Ocean plate led to another magmatic "flare-up" in the southern margin of the Lhasa terrane [24,68]. In summary, this study suggests that the Late Cretaceous granodiorite formed under the dynamic background of the Neo-Tethys Ocean slab rollback (Figure 13a).

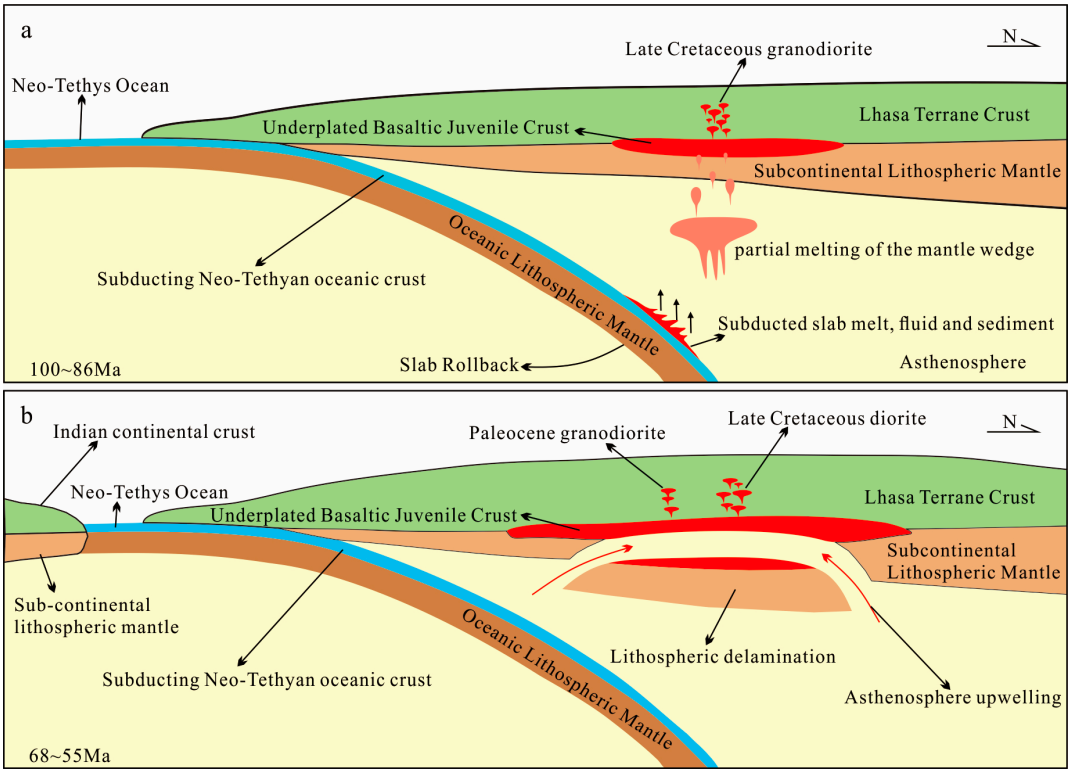


Figure 13. Tectonic model for the western segment of the southern margin of the Lhasa terrane at 100–86 Ma (**a**) and 68–55 Ma (**b**).

There are numerous intrusive rocks aged 68~60 Ma in the southern margin of the Lhasa terrane, and their formation mechanisms remain controversial. Both slab rollback and lithospheric delamination can lead to extensive magmatic activity, as these processes can cause upwelling of the asthenospheric mantle and provide the necessary heat for magma formation [83]. Zhu et al. [76] proposed that the rollback of the Neo-Tethyan slab, commencing at ~70 Ma prior to the India–Asia collision, served as a key geodynamic process responsible for regional thermal perturbations and the compositional transition of magmatism. In this study, we contend that the Late Cretaceous diorites in the Qiuwo area, southern Lhasa Terrane, were generated in response to this pre-collisional tectonic transition, specifically within a dynamic context of lithospheric delamination. (Figure 7b,

Stage 3; Figure 13b). Lithospheric delamination is an important and relatively common component in collisional orogenic processes [84,85]. The magmatic underplating process involves the ascent and subsequent stagnation of basaltic magmas derived from the mantle at the base of the lower crust, leading to its thickening. This thickened lower crust promotes the transformation of granulite-facies lower crust into eclogite-facies rocks, resulting in a significant increase in rock density. The resultant gravitational instability of the lower crust can ultimately trigger lithospheric delamination [86,87]. This delamination can cause upwelling of the asthenospheric mantle and decompression partial melting, providing the necessary heat for lithospheric melting [88]. The evidence is presented in the following three paragraphs, supporting this view.

(1) The Sr/Y and $(La/Yb)_N$ values of the magmatic rocks after 69 Ma are low. The Sr/Y and $(La/Yb)_N$ values of magmatic rocks are controlled by the stability of specific minerals (such as garnet, amphibole, and plagioclase) in the magma source at a certain depth during partial melting [89]. If the melt originates from deep partial melting, where garnet is stable and plagioclase is unstable, the resulting magma will have high Sr/Y and $(La/Yb)_N$ values; if partial melting occurs at shallow depths, it will result in lower Sr/Y and $(La/Yb)_N$ values [25,48]. The late diorite of the Late Cretaceous in the Qiuwo area have Sr/Y and $(La/Yb)_N$ values ranging from 27.18 to 32.86 (average 29.68) and from 9.33929362 to 10.6850337 (average 9.795840372), respectively, indicating that the magma source was relatively shallow. Between 85 and 73 Ma, the Sr/Y and $(La/Yb)_N$ ratios of the intrusions gradually increased over time, indicating a progressive deepening of the magma source. However, after the magmatic hiatus from 73 to 69 Ma, these ratios decreased sharply, suggesting the occurrence of lithospheric delamination along the southern margin of the Lhasa terrane [24,25]. The Late Cretaceous diorites in the Qiuwo area exhibit relatively low Sr/Y (average 29.68) and $(La/Yb)_N$ (average 9.80) values, which indicate a relatively shallow magma source and support their formation in a tectonic setting associated with lithospheric delamination.

(2) The $Mg^{\#}$ values of the 68~60 Ma intrusive rocks show significant variation. Lithospheric delamination can cause upwelling of the asthenosphere and decompression partial melting, leading to the interaction of magma with mantle peridotite and the formation of high $Mg^{\#}$ melts [86]. Most samples from the 68–60 Ma magmatic activity have low $Mg^{\#}$ values (<50), indicating that these intrusions, including the Late Cretaceous diorite in the Qiuwo area, were formed by partial melting of the un-delaminated juvenile crust. However, some samples have high $Mg^{\#}$ values (50~64), suggesting that these high $Mg^{\#}$ samples may have been formed by partial melting of the delaminated lithosphere and interacted with mantle peridotite during magma ascent.

(3) The magma temperatures of the 68~60 Ma intrusive rocks are anomalous. The magmatic temperatures recorded in the Late Cretaceous diorite from the Qiuwo area are comparable to those (755–676 °C) of the regional 68–60 Ma magmatic activity (755~676 °C) [25], while the magma temperatures from 85~74 Ma are 628~685 °C [25]. Under conditions of constant crustal thickness and geothermal gradient, deeper magma sources would have higher temperatures. The magma source for the Late Cretaceous diorite is shallower than that of the 85~74 Ma intrusions, yet it has a higher magma temperature than the 85~74 Ma intrusions. This anomalous phenomenon is due to lithospheric delamination, which causes the upwelling of high-temperature asthenospheric material to fill the space vacated by the delaminated lithosphere, providing heat to the lower crust and resulting in the anomalous magma temperatures.

The Paleocene granodiorite in the Qiuwo area of the southern margin of the Lhasa terrane exhibit distinct arc magmatic characteristics, indicating that they were still in a

subduction tectonic setting. Figure 7b shows that the 57 Ma granodiorite was emplaced during a magmatic lull between two activity peaks. In light of regional magmatic records, magmatism in the southern Lhasa Terrane shows an overall waning trend after the ~68 Ma lithospheric delamination event. This pattern likely reflects the gradual decay of the thermal perturbation triggered by lithospheric delamination, while sustained slab rollback served as the principal geodynamic mechanism maintaining magmatic activity during this period [76]. In the Y-Nb, Y + Nb-Rb, and Yb + Ta-Rb diagrams (Figure 12), the Paleocene granodiorite and coeval magmatic rocks in the Qiuwo area fall within the volcanic arc granite field, indicating that the rock bodies formed before the collision between the Indian and Eurasian continents. Additionally, during the collision process, slab break-off would cause upwelling of the asthenosphere, which would be reflected in the magmatic evolution as more depleted isotopic compositions [3,56]. The $\varepsilon_{Hf}(t)$ values of the Paleocene granodiorite range from +4.02 to +5.90 (average +4.91), with $(^{87}Sr/^{86}Sr)_i$ values ranging from 0.705460 to 0.705469 and $\varepsilon_{Hf}(t)$ values ranging from −0.43 to −0.11. These isotopic characteristics indicate that the granodiorites were derived from partial melting of juvenile basaltic lower crust with the addition of ancient crustal material, which does not match the depleted mantle magmatic characteristics formed by slab break-off. This also suggests that the granodiorites formed before the collision between the Indian and Eurasian continents (Figure 13b).

6. Conclusions

(1) The formation ages of the three phases of intermediate to acidic intrusive rocks in the Qiuwo area are 89.9 Ma (Late Cretaceous granodiorite), 68.6 Ma (Late Cretaceous diorite), and 56.75 Ma (Granodiorite of the Paleocene).

(2) The three phases of intermediate to acidic intrusive rocks in the Qiuwo area of the southern margin of the Lhasa terrane are all undifferentiated I-type granitic rocks.

(3) The three phases of intermediate to acidic intrusive rocks in the Qiuwo area of the southern margin of the Lhasa terrane were formed by the partial melting of juvenile basaltic lower crustal rocks. From the early Late Cretaceous to the Paleocene, the magmatic activity in the southern margin of the Lhasa terrane incorporated an increasing amount of ancient crustal material, and the intrusions experienced a certain degree of fractional crystallization during emplacement.

(4) The early granodiorite of the Late Cretaceous was formed in a tectonic setting related to the rollback of the subducting Neo-Tethyan slab. The late diorite of the Late Cretaceous and Eocene granodiorite were associated with lithospheric delamination after 68 Ma, with the Granodiorite of the Paleocene exhibiting typical arc magmatic geochemical characteristics, indicating that the India–Eurasia collision occurred after its formation.

Supplementary Materials: The following supporting information can be downloaded at: https://www.mdpi.com/article/10.3390/min16010063/s1, Table S1. Zircon LA-ICP-MS U-Pb Geochronology of Intermediate–Acid Intrusive Rocks in the Qiuwo Area, Southern Margin of the Lhasa Terrane; Table S2. Major (wt.%), Rare Earth Element (REE), and Trace Element ($\times 10^{-6}$) Geochemistry of the Intermediate–Acid Intrusive Rocks in the Qiuwo Area, Southern Margin of the Lhasa Terrane; Table S3. Zircon Lu-Hf Isotopic Composition of the Intermediate–Acid Intrusive Rocks from the Qiuwo Area, Southern Margin of the Lhasa Terrane; Table S4. Whole-rock Sr-Nd Isotopic Composition of the Intermediate–Acid Intrusive Rocks from the Qiuba Area, Southern Margin of the Lhasa Terrane.

Author Contributions: M.J.: Investigation, Formal analysis, Writing—Original Draft, Writing—Review & Editing. Y.L., S.C., Y.Y. and J.L.: Investigation, Formal analysis. F.X.: Investigation,

Project administration, Supervision. All authors have read and agreed to the published version of the manuscript.

Funding: This work was supported by the [National Key Research and Development Program of China] under Grant [number 2022YFC2905002]; [Sichuan Provincial Natural Science Foundation Project] under Grant [number 2025ZNSFSC1197]; and [Chengdu University of Technology Summit Scientific Research Program Project] under Grant [number 2024ZF11426].

Data Availability Statement: Data are contained within the article.

Acknowledgments: Special thanks are given to the anonymous reviewers for their critical and constructive reviews.

Conflicts of Interest: Authors Yibin Lin, Shuyuan Chen, Yang Yang and Jiancuo Luosang were employed by the Tibet Xianglong Mining Co., Ltd. The remaining authors declare that the research was conducted in the absence of any commercial or financial relationships that could be construed as a potential conflict of interest.

References

1. Wu, F.Y.; Li, X.H.; Yang, J.H.; Zheng, Y.F. Discussions on the petrogenesis of granites. *Acta Petrol. Sin.* **2007**, *23*, 1217–1238. (In Chinese, with English Abstract)
2. Rudnick, R.L. Making continental crust. *Nature* **1995**, *378*, 571–578. [CrossRef]
3. Mo, X.X.; Hou, Z.Q.; Niu, Y.L.; Dong, G.C.; Qu, X.M.; Zhao, Z.D.; Yang, Z.M. Mantle contributions to crustal thickening during continental collision: Evidence from Cenozoic igneous rocks in southern Tibet. *Lithos* **2007**, *96*, 225–242. [CrossRef]
4. Mo, X.X.; Dong, G.C.; Zhao, Z.D.; Zhou, S.; Wang, L.L.; Qiu, R.Z.; Zhang, F.Q. Spatial and Temporal Distribution and Characteristics of Granitoids in the Gangdese, Tibet and Implication for Crustal Growth and Evolution. *Geol. J. China Univ.* **2005**, *11*, 281–290. (In Chinese with English Abstract)
5. Zhu, D.H.; Wang, Q.; Weinberg, R.F.; Cawood, P.A.; Zhao, Z.D.; Hou, Z.Q.; Mo, X.X. Continental Crustal Growth Processes Recorded in the Gangdese Batholith, Southern Tibet. *Rev. Artic.* **2023**, *51*, 155–188. [CrossRef]
6. Zhang, Z.M.; Ding, H.X.; Palin, R.M.; Dong, X.; Tian, Z.L.; Li, X.W. Crustal evolution of a continental magmatic arc from subduction to collision: A case study in the Gangdese arc, southern Tibetan Plateau. *GSA Bull.* **2024**, *136*, 4059–4071. [CrossRef]
7. Dong, M.C. Chronology and Geochemistry of Late Cretaceous Granites in Southern Lhasa Terrane. Ph.D. Thesis, China University of Geosciences, Beijing, China, 2017. (In Chinese with English Abstract)
8. Zhu, D.C.; Zhao, Z.D.; Niu, Y.; Mo, X.X.; Chung, S.L.; Hou, Z.Q.; Wang, L.Q.; Wu, F.Y. The Lhasa Terrane: Record of a microcontinent and its histories of drift and growth. *Earth Planet. Sci. Lett.* **2011**, *301*, 241–255. [CrossRef]
9. Ji, W.Q.; Wu, F.Y.; Zhong, S.L.; Liu, C.Z. Geochronology and Petrogenesis of Granitic Rocks in Gangdese Batholith, Southern Tibet. *Sci. China Ser. D Earth Sci.* **2009**, *39*, 849–871. (In Chinese with English abstract)
10. Lee, H.Y.; Chung, S.L.; Lo, C.H.; Ji, J.Q.; Lee, T.Y.; Qian, Q.; Zhang, Q. Eocene Neotethyan slab breakoff in southern Tibet inferred from the Linzizong volcanic record. *Tectonophysics* **2009**, *477*, 20–35. [CrossRef]
11. Dong, G.C.; Mo, X.X.; Zhao, Z.D.; Wang, L.L.; Chen, T. A Coupling Model of Rigid-block Movement and Continuous Deformation:Patterns of the Present day Deformation of China's Continent and Its Vicinity. *Acta Geol. Sin.* **2005**, *79*, 756. (In Chinese with English Abstract)
12. Mo, X.X.; Zhao, Z.D.; Deng, J.F.; Dong, G.C.; Zhou, S.; Guo, T.Y.; Zhang, S.Q.; Wang, L.L. Response of Volcanism to the India-asia Collision. *Geosci. Front.* **2003**, *10*, 135–148. (In Chinese with English Abstract)
13. Yin, A.; Harrison, T.M. Geologic evolution of the Himalayan-Tibetan Orogen. *Annu. Rev. Earth Planet. Sci.* **2000**, *28*, 211–280. [CrossRef]
14. Zhu, D.C.; Wang, Q.; Zhao, Z.D.; Chung, S.L.; Cawood, P.A.; Niu, Y.L.; Liu, S.A.; Wu, F.Y.; Mo, X.X. Magmatic record of lndia-Asia collision. *Sci. Rep.* **2015**, *5*, srep14289.
15. Ma, L.; Wang, Q.; Wyman, D.A.; Li, Z.X.; Jiang, Z.Q.; Yang, J.H.; Gou, G.N.; Gou, H.F. Late Cretaceous (100~89 Ma) magnesian charnockites with adakitic affinities in the Milin area, eastern Gangdese: Partial melting of subducted oceanic crust and implications for crustal growth in southern Tibet. *Lithos* **2013**, *175–176*, 315–332. [CrossRef]
16. Ma, L.; Wang, Q.; Wyman, D.A.; Jiang, Z.Q.; Yang, J.H.; Li, Q.L.; Gou, G.N.; Gou, H.F. Late Cretaceous crustal growth in the Gangdese area, southern Tibet: Petrological and Sr-Nd-Hf-O isotopic evidence from Zhengga diorite-gabbro. *Chem. Geol.* **2013**, *349–350*, 54–70.

17. Ma, L.; Wang, Q.; Li, Z.X.; Wyman, D.A.; Jiang, Z.Q.; Yang, J.H.; Gou, G.N.; Gou, H.F. Early Late Cretaceous (ca. 93Ma) norites and hornblendites in the Milin area, eastern Gangdese: Lithosphere-asthenosphere interaction during slab roll-back and an insight into early Late Cretaceous (ca. 100~80 Ma) magmatic "flare-up" in southern Lhasa (Tibet). *Lithos* **2013**, *172–173*, 17–30.
18. Jiang, Z.Q.; Wang, Q.; Wyman, D.A.; Li, Z.X.; Yang, J.H.; Shi, X.B.; Ma, L.; Tang, G.J.; Gou, G.N.; Jia, X.H.; et al. Transition from oceanic to continental lithosphere subduction in southern Tibet: Evidence from the Late Cretaceous–Early Oligocene (~91–30 Ma) intrusive rocks in the Chanang–Zedong area, southern Gangdese. *Lithos* **2014**, *196–197*, 213–231.
19. Chen, L.; Qin, K.Z.; Li, G.M.; Li, J.X.; Xiao, B.; Zhao, J.X.; Fan, X. Zircon U-Pb ages, geochemistry, and Sr-Nd-Pb-Hf isotopes of the Nuri intrusive rocks in the Gangdese area, southern Tibet: Constraints on timing, petrogenesis, and tectonic transformation. *Lithos* **2015**, *212–215*, 379–396.
20. Zhang, H.; Harris, N.; Guo, L.; Xu, W.C. The significance of Cenozoic magmatism from the western margin of the eastern syntaxis, southeast Tibet. *Contrib. Mineral. Petrol.* **2010**, *160*, 83–98.
21. Zheng, Y.C.; Hou, Z.Q.; Gong, Y.L.; Liang, W.; Sun, Q.Z.; Zhang, S.; Fu, Q.; Huang, K.X.; Li, Q.Y.; Li, W. Petrogenesis of Cretaceous adakite-like intrusions of the Gangdese Plutonic Belt, southern Tibet: Implications for mid-ocean ridge subduction and crustal growth. *Lithos* **2014**, *190–191*, 240–263.
22. Wen, D.R.; Chung, S.L.; Song, B.; Iizuka, Y.; Yang, H.J.; Ji, J.Q.; Liu, D.Y.; Gallet, S. Late Cretaceous Gangdese intrusions of adakitic geochemical characteristics, SE Tibet: Petrogenesis and tectonic implications. *Lithos* **2008**, *105*, 1–11. [CrossRef]
23. Wen, D.R.; Liu, D.Y.; Chung, S.L.; Chu, M.F.; Ji, J.Q.; Zhang, Q.; Song, B.; Lee, T.Y.; Yeh, M.W.; Lo, C.H. Zircon SHRIMP U-Pb ages of the Gangdese Batholith and implications for Neotethyan subduction in southern Tibet. *Chem. Geol.* **2008**, *252*, 191–201.
24. Xie, F.W.; Lang, X.H.; Tang, J.X.; Ma, D.; Zou, B. Late Cretaceous magmatic activity in the southern Lhasa terrane: Insights from the Dazhuqu hornblende gabbro and the Xietongmen granite porphyry. *Int. Geol. Rev.* **2019**, *61*, 1642–1665.
25. Ji, W.Q.; Wu, F.Y.; Chung, S.L.; Liu, C.Z. The Gangdese magmatic constraints on a latest Cretaceous lithospheric delamination of the Lhasa terrane, southern Tibet. *Lithos* **2014**, *210*, 168–180. [CrossRef]
26. Pearce, J.A.; Deng, W.M. The ophiolites of the Tibetan Geotraverses, Lhasa to Golmud (1985) and Lhasa to Kathmandu (1986). *Philos. Trans. R. Soc.* **1988**, *327*, 215–238.
27. Dong, X.; Zhang, Z.; Santosh, M. Zircon U-Pb chronology of the Nyingtri group, southern Lhasa terrane, Tibetan Plateau: Implications for Grenvillian and Pan-African provenance and Mesozoic-Cenozoic metamorphism. *J. Geol.* **2010**, *118*, 677–690.
28. Zhu, D.C.; Zhao, Z.D.; Niu, Y.L.; Dilek, Y.; Hou, Z.Q.; Mo, X.X. The origin and pre-Cenozoic evolution of the Tibetan Plateau. *Gondwana Res.* **2013**, *23*, 1429–1454. [CrossRef]
29. Zhu, J.; Liu, Z.X.; Zhang, H.J.; Tian, W.X.; Li, X.W.; Tan, M.T.; Li, Z.H.; Gong, Z.Y. *1:250,000 Regional Geological Survey of Lhazê County Sheet, Tibet*; Hubei Institute of Geological Survey: Wuhan, China, 2003. (In Chinese with English Abstract)
30. Liu, Y.S.; Hu, Z.C.; Zong, K.Q.; Gao, C.G.; Gao, S.; Xu, J.; Chen, H.H. Reappraisement and Refinement of Zircon U-Pb Isotope and Trace Element Analyses by LA-ICP-MS. *Chin. Sci. Bull.* **2010**, *55*, 1535–1546. [CrossRef]
31. Wu, F.Y.; Yang, Y.H.; Xie, L.W.; Yang, J.H.; Xu, P. Hf isotopic compositions of the standard zircons and baddeleyites used in U-Pb geochronology. *Chem. Geol.* **2006**, *234*, 105–126.
32. Weis, D.; Kieffer, B.; Maerschalk, C.; Barling, J.; Jong, J.D.; Williams, G.A.; Hanano, D.; Pretorius, W.; Mattielli, N.; Scoates, J.S.; et al. High-precision isotopic characterization of USGS reference materials by TIMS and MC-ICP-MS. *Geochem. Geophys. Geosystems* **2006**, *7*, 139–149.
33. Weis, D.; Kieffer, B.; Hanano, D.; Silva, I.N.; Barling, J.; Pretorius, W.; Maerschalk, C.; Mattielli, N. Hf isotope compositions of U.S. geological survey reference materials. *Geochem. Geophys. Geosystems* **2007**, *8*, 6. [CrossRef]
34. Rubatto, D. Zircon Trace Element Geochemistry: Partitioning with Garnet and the Link Between U-Pb Ages and Metamorphism. *Chem. Geol.* **2002**, *184*, 123–138. [CrossRef]
35. Middlemost, E.A.K. Naming materials in the magma/igneous rock system. *Earth-Sci. Rev.* **1994**, *37*, 215–224. [CrossRef]
36. Peccerillo, A.; Taylor, S.R. Geochemistry of Eocene calcalkaline volcanic rocks from the Kastamonu area, northernTurkey. *Contrib. Mineral. Petrol.* **1976**, *58*, 63–81. [CrossRef]
37. Maniar, P.D.; Piccoli, P.M. Tectonic discrimination of granitoids. *Geol. Soc. Am. Bull.* **1989**, *101*, 635–643.
38. Tang, M.; Wang, X.L.; Shu, X.J.; Wang, D.; Yang, T.; Gopon, P. Hafnium isotopic heterogeneity in zircons from granitic rocks: Geochemical evaluation and modeling of "zircon effect" in crustal anatexis. *Earth Planet. Sci. Lett.* **2014**, *389*, 188–199. [CrossRef]
39. Xu, W.C.; Zhang, H.F.; Luo, B.J.; Guo, L.; Yang, H. Adakite-like geochemical signature produced by amphibole-dominated fractionation of arc magmas: An example from the Late Cretaceous magmatism in Gangdese belt, south Tibet. *Lithos* **2015**, *232*, 197–210. [CrossRef]
40. Wen, D.R. The Gangdese Batholith, Southern Tibet: Ages, Geochemical Characteristics and Petrogenesis. Ph.D. Thesis, National Taiwan University, Taipei, China, 2007.
41. Jiang, Z.Q.; Wang, Q.; Li, Z.X.; Wyman, D.A.; Tang, G.J.; Jia, X.H.; Yang, Y.H. Late Cretaceous (ca. 90Ma) adakitic intrusive rocks in the Kelu area, Gangdese belt (southern Tibet): Slab melting and implications for Cu-Au mineralization. *J. Asian Earth Sci.* **2012**, *53*, 67–81.

42. Zhang, L.L.; Liu, C.Z.; Wu, F.Y.; Ji, W.Q.; Wang, J.G. Zedong terrane revisited: An intraoceanic arc within Neo-Tethys or a part of the Asian active continental margin? *J. Asian Earth Sci.* **2014**, *80*, 34–55.
43. Zhang, L.L.; Liu, C.Z.; Wu, F.Y.; Zhang, C.; Ji, W.Q.; Wang, J.G. Sr-Nd-Hf isotopes of the intrusive rocks in the Cretaceous Xigaze ophiolite, southern Tibet: Constraints on its formation setting. *Lithos* **2016**, *258–259*, 133–148.
44. Huang, F.; Li, M.J.; Xu, J.F.; Zeng, Y.C.; Chen, J.L.; Wang, B.D.; Yu, H.X.; Chen, L.; Zhao, P.P.; Zhang, Z. Geodynamic transition from subduction to extension: Evidence from the geochronology and geochemistry of granitoids in the Sangsang area, southern Lhasa Terrane, Tibet. *Int. J. Earth Sci.* **2019**, *108*, 1663–1681. [CrossRef]
45. Zhou, L.M.; Wang, R.; Hou, Z.Q.; Li, C.; Zhao, H.; Li, X.W.; Qu, W.J. Hot Paleocene-Eocene Gangdese arc: Growth of continental crust in southern Tibet. *Gondwana Res.* **2018**, *62*, 178–197. [CrossRef]
46. Wang, R.; Richards, J.P.; Hou, Z.Q.; An, F.; Creaser, R.A. Zircon U-Pb age and Sr-Nd-Hf-O isotope geochemistry of the Paleocene-Eocene igneous rocks in western Gangdese: Evidence for the timing of Neo-Tethyan slab breakoff. *Lithos* **2015**, *224–225*, 179–194. [CrossRef]
47. Wang, R.; Richards, J.P.; Zhou, L.M.; Hou, Z.Q.; Stern, R.A.; Creaser, R.A.; Zhu, J.J. The role of Indian and Tibetan lithosphere in spatial distribution of Cenozoic magmatism and porphyry Cu-Mo deposits in the Gangdese belt, southern Tibet. *Earth-Sci. Rev.* **2015**, *150*, 68–94. [CrossRef]
48. Ji, W.Q.; Wu, F.Y.; Liu, C.Z.; Chung, S.L. Early Eocene crustal thickening in southern Tibet: New age and geochemical constraints from the Gangdese batholith. *J. Asian Earth Sci.* **2012**, *53*, 82–95. [CrossRef]
49. Huang, Y.; Zhao, Z.D.; Zhang, F.Q.; Zhu, D.C.; Dong, G.C.; Zhou, S.; Mo, X.X. Geochemistry and Implication of the Gangdese Batholiths from Renbu and Lhasa Areas in Southern Gangdese, Tibet. *Acta Petrol. Sin.* **2010**, *26*, 3131–3142. (In Chinese with English Abstract)
50. Xu, W.C.; Zhang, H.F.; Guo, L.; Yuan, H.L. Miocene high Sr/Y magmatism, south Tibet: Product of partial melting of subducted Indian continental crust and its tectonic implication. *Lithos* **2010**, *114*, 293–306. [CrossRef]
51. Mo, X.X.; Niu, Y.L.; Dong, G.C.; Zhao, Z.D.; Hou, Z.Q.; Zhou, S.; Ke, S. Contribution of syncollisional felsic magmatism to continental crust growth: A case study of the Paleogene Linzizong volcanic Succession in southern Tibet. *Chem. Geol.* **2008**, *250*, 49–67. [CrossRef]
52. Sun, S.S.; McDonough, W.F. Chemical and isotopic systematics of oceanic basalts: Implications for mantle composition and processes. *Geol. Soc. Lond. Spec. Publ.* **1989**, *42*, 313–345.
53. Schärer, U.; Xu, R.H.; Allegre, C.J. U-Pb geochronology of Gangdese (Transhimalaya) plutonism in the Lhasa-Xigaze region, Tibet. *Earth Planet. Sci. Lett.* **1984**, *69*, 311–320.
54. Mo, X.X.; Dong, G.C.; Zhao, Z.D.; Zhu, D.C.; Zhou, S.; Niu, Y.L. Mantle input to the crust in southern Gangdese, Tibet, during the Cenozoic: Zircon Hf isotopic evidence. *J. Earth Sci.* **2009**, *20*, 241–249. [CrossRef]
55. Chung, S.L.; Chu, M.F.; Zhang, Y.Q.; Xie, Y.W.; Lo, C.H.; Lee, T.Y.; Lan, C.Y.; Li, X.H.; Zhang, Q.; Wang, Y.Z. Tibetan tectonic evolution inferred from spatial and temporal variations in postcollisional magmatism. *Earth-Sci. Rev.* **2005**, *68*, 173–196. [CrossRef]
56. Ma, X.X.; Meert, J.G.; Xu, Z.Q.; Zhao, Z.B. Evidence of magma mixing identified in the Early Eocene Cainapluton from the Gangdese batholith southern Tibet. *Lithos* **2017**, *278–281*, 126–139. [CrossRef]
57. Clemens, J.D. S-type granitic magmas—Petrogenetic issues, models and evidence. *Earth-Sci. Rev.* **2003**, *61*, 1–18. [CrossRef]
58. Watson, E.B.; Harrison, T.M. Zircon saturation revisited:temperature and composition effectsin a variety of crustal magma types. *Earth Planet. Sci. Lett.* **1983**, *64*, 295–304. [CrossRef]
59. Whalen, J.B.; Currie, K.L.; Chappell, B.W. A-type granites: Geochemical characteristics, discrimination and petrogenesis. *Contrib. Mineral. Petrol.* **1987**, *95*, 407–419. [CrossRef]
60. Cao, H.H. Geochronology and Geochemistry of the Late Paleozoic-EarlyMesozoic Igneous Rocks in the Eastern Segment of the Northernmargin of the North China Block. Ph.D. Thesis, Jilin University, Changchun, China, 2013. (In Chinese with English Abstract)
61. Shinjo, R.; Kato, Y. Geochemical constraints on the origin of bimodal magmatism at the Okinawa Trough, an incipient back-arc basin. *Lithos* **2000**, *54*, 117–137. [CrossRef]
62. Bonin, B. Do coeval mafic and felsic magmas in post-collisional to within-plate regimes necessarily imply two contrasting, mantle and crustal, sources? A review. *Lithos* **2004**, *78*, 1–24. [CrossRef]
63. Frost, C.D.; Frost, B.R.; Chamberlain, K.R.; Edwards, B.R. Petrogenesis of the 1.43 Ga Sherman batholith, SE Wyoming, USA: A reduced, rapakivi-type anorogenic granite. *J. Petrol.* **1999**, *40*, 1771–1802. [CrossRef]
64. Foland, K.A.; Allen, J.C. Magma sources for Mesozoic anorogenic granites of the White Mountain magma series, New England, USA. *Contrib. Mineral. Petrol.* **1991**, *109*, 195–211. [CrossRef]
65. Rapp, R.P.; Watson, E.B. Dehydration Melting of Metabasalt at 8–32 kbar: Implications for Continental Growth and Crust-Mantle Recycling. *J. Petrol.* **1995**, *36*, 891–931. [CrossRef]
66. Defant, M.J.; Drummond, M.S. Derivation of some modern arc magmas by melting of young subducted lithosphere. *Nature* **1990**, *347*, 662–665. [CrossRef]

67. Ma, L.; Wang, Q.; Wyman, D.A.; Jiang, Z.Q.; Wu, F.Y.; Li, X.H.; Yang, J.H.; Gou, G.N.; Gou, H.F. Late Cretaceous back-arc extension and arc system evolution in the Gangdese area, southern Tibet: Geochronological, petrological, and Sr-Nd-Hf-O isotopic evidence from Dagze diabases. *J. Geophys. Res. Solid Earth* **2015**, *120*, 6159–6181. [CrossRef]
68. Ji, W.Q.; Wu, F.Y.; Chung, S.L.; Li, J.X.; Liu, C.Z. Zircon U-Pb geochronology and Hf isotopic constraints on petrogenesis of the Gangdese batholith, southern Tibet. *Chem. Geol.* **2009**, *262*, 229–245. [CrossRef]
69. Sharifi, A.; Murphy, L.N.; Pourmand, A.; Clement, A.C.; Canuel, E.A.; Beni, A.N.; Lahijani, H.A.K.; Delanghe, D.; Ahmady-Birgani, H. Early-Holocene greening of the Afro-Asian dust belt changed sources of mineral dust in West Asia. *Earth Planet. Sci. Lett.* **2018**, *481*, 30–40. [CrossRef]
70. Luo, C. Geochemical Characteristics and Tectonic Significance of Yemaquan Granodiorite in Ejina Banner, Inner Mongolia. Master's Thesis, Hebei GEO University, Shijiazhuang, China, 2021. (In Chinese with English Abstract)
71. Shao, J.A.; Mu, B.L.; Zhu, H.Z.; Zhang, L.Q. Material Source and Tectonic Settings of the Mesozoic Mineralization of the Da Hinggan Mts. *Acta Petrol. Sin.* **2010**, *26*, 649–656. (In Chinese with English Abstract)
72. Zhao, Z.H. *Geochemistry of Trace Elements*; Beijing Science Press: Beijing, China, 2016. (In Chinese with English Abstract)
73. Wang, L.Y.; Peng, X.D.; Huang, L.L.; Lin, M.S.; Zhang, W.H. Petrogenesis and Geological Implications of the Changanshan Diorite and Rhyolite in Minhou Area, Fuzhou. *Acta Petrol. Sin.* **2020**, *36*, 1833–1849. (In Chinese with English abstract)
74. Hildreth, W.; Moorbath, S. Crustal contributions to arc magmatism in the Andes of central Chile. *Contrib. Mineral. Petrol.* **1988**, *98*, 455–489. [CrossRef]
75. Pearce, J.A.; Harris, N.B.W.; Tindle, A.G. Trace element discrimination diagrams for the tectonic interpretation of granitic rocks. *J. Petrol.* **1984**, *25*, 956–983. [CrossRef]
76. Zhu, D.C.; Wang, Q.; Weinberg, R.F.; Cawood, P.A.; Chung, S.L.; Zheng, Y.F.; Zhao, Z.D.; Hou, Z.Q.; Mo, X.X. Interplay between oceanic subduction and continental collision in building continental crust. *Nat. Commun.* **2022**, *13*, 7141. [CrossRef] [PubMed]
77. Ducea, M.N.; Barton, M.D. Igniting flare-up events in Cordilleran arcs. *Geology* **2007**, *35*, 1047–1050. [CrossRef]
78. Guo, L.; Zhang, H.F.; Harris, N.; Pan, F.B.; Xu, W.C. Late Cretaceous (~81 Ma) high-temperature metamorphism in the southeastern Lhasa terrane: Implication for the NeoTethys ocean ridge subduction. *Tectonophysics* **2013**, *608*, 112–126. [CrossRef]
79. Cole, R.B.; Stewart, B.W. Continental margin volcanism at sites of spreading ridge subduction: Examples from southern Alaska and western California. *Tectonophysics* **2009**, *464*, 118–136. [CrossRef]
80. Lai, K. Late Cretaeous Magmatism in the CentralGangdese Arc, Tibet, and Its Implication for the Growth of Continental Crust. Ph.D. Thesis, China University of Geosciences, Wuhan, China, 2023. (In Chinese with English Abstract)
81. Gianni, G.M.; Luján, S.P. Geodynamic controls on magmatic arc migration and quiescence. *Earth-Sci. Rev.* **2021**, *218*, 103676. [CrossRef]
82. Ma, X.; Attia, S.; Cawood, T.; Cao, W.R.; Xu, Z.Q.; Li, H.B. Arc tempos of the Gangdese batholith, southern Tibet. *J. Geodyn.* **2022**, *149*, 101897. [CrossRef]
83. Bird, P. Continental delamination and the Colorado Plateau. *J. Geophys. Res. Solid Earth* **1979**, *84*, 7561–7571. [CrossRef]
84. Zhu, D.C.; Wang, Q.; Li, S.M.; Zhan, Q.Y.; Liu, Z.; Xie, J.C.; Liu, L.; Zhang, L.L.; Zhong, X.Y.; Zhao, Y.X. Magma genesis and crustal evolution in continental collision zones. *Sci. China Earth Sci.* **2025**, *68*, 1346–1370. [CrossRef]
85. Nelson, K.D. Are crustal thickness variations in oldmountain belts like the Appalachians a consequence oflithospheric delamination? *Geology* **1992**, *20*, 498–502. [CrossRef]
86. Gao, S.; Rudnick, R.L.; Yuan, H.L.; Liu, X.M.; Liu, Y.S.; Xu, W.L.; Ling, W.L.; Ayers, J.; Wang, X.C.; Wang, Q.H. Recycling lower continental crust in the North China craton. *Nature* **2004**, *432*, 892–897. [CrossRef] [PubMed]
87. Kay, R.W.; Kay, S.M. Creation and destruction of lower continental crust. *Geol. Rundsch.* **1991**, *80*, 259–278. [CrossRef]
88. Kay, R.W.; Kay, S.M. Delamination and delamination magmatism. *Tectonophysics* **1993**, *219*, 177–189. [CrossRef]
89. Shen, P.; Shen, Y.C.; Liu, T.B.; Meng, L.; Dai, H.W.; Yang, Y.H. Geochemical signature of porphyries in the Baogutu porphyry copper belt, Western Junggar, NW China. *Gondwana Res.* **2009**, *16*, 227–242. [CrossRef]

Disclaimer/Publisher's Note: The statements, opinions and data contained in all publications are solely those of the individual author(s) and contributor(s) and not of MDPI and/or the editor(s). MDPI and/or the editor(s) disclaim responsibility for any injury to people or property resulting from any ideas, methods, instructions or products referred to in the content.